Positron annihilation spectroscopy of ion-implanted and laser-irradiated semiconductors

Malik, Farhad

Award date:
2000

Awarding institution:
University of Bath

Positron Annihilation Spectroscopy of Ion-Implanted and Laser-Irradiated Semiconductors

Farhad Malik

2000

Submitted in partial fulfilment of the requirements for the degree of

Doctor of Philosophy at the University of Bath

ProQuest LLC
789 East Eisenhower Parkway
P.O. Box 1346
Ann Arbor, MI 48106-1346

Abstract

Positron Annihilation Spectroscopy (PAS) has been used to study the nature of sub-surface defects in a host of semi-conducting materials, combining conventional Doppler broadening spectroscopy with novel techniques to elucidate fresh information on the systems studied.

FZ(Float Zone)-Si doped with 5keV B^+ at ion fluences between 2×10^{12} to 2×10^{15} cm^{-2} was investigated for structural damage. Ion depth profiles determined by SIMS exhibited tails extending well beyond the limit predicted by the simulation code TRIM, attributed to ion channelling. PAS, when extended by repeated measurements after precise anodic etching of 40 and 140nm of material, showed that the vacancy-type defect depth profiles also extended far beyond the limit predicted by TRIM.

The annihilation linewidth parameter S has been measured for n-type FZ-Si(100) implanted with 50 keV As^+, 5 keV B^+, 120 keV Ge^+, 450 keV H^+, 200 keV He^+, 400 keV O^+ and 125 keV Si^+ ions. Maximum values of S can be normalised to a single, well-defined distribution using vacancy concentrations given by TRIM, indicating that the vacancy-type defects from these implantations are similar in both structure and interstitial combination rate.

An ex-situ annealing study of vacancy-type defects in Si created by 50 keV Si^+ implantation has suggested that the threshold temperature for the migration of the defects, $\sim 500^oC$ is higher than expected for divacancy annealing, implying the formation of some form of divacancy-impurity complex. A novel in-situ annealing technique has been developed to investigate this migration regime.

PAS studies of laser irradiated 4H-SiC has indicated the existence of subsurface damage consistent with the formation of vacancy agglomerates. This occurs at higher fluences (above 1.2 Jcm^{-2}) of 308nm radiation, but at all fluences used at 193nm for which direct bond-breaking is attributed.

Acknowledgements

There are a lot of people out there that thanks has to be given to. First and foremost has to be my parents without whom I wouldn't have existed. They've also kept me on the straight and narrow path so that I would become good marriage material. A mention also for the rest of my family, brothers and sisters in Wales and Leeds. Stay Jawaan.

I've also met some top people whilst at university, so a big shout out to Foster, Phil, Suzie Q, Nom, Jon, Ben, Suzie T, Nick, Mike C, Chris W and all you others that I will never forget but can't quite remember your names at the moment. You've made my life very enjoyable and hence made the work pass more easily.

There have been plenty of people in the physics department, both at Bath and UEA, that have helped me out immeasurably, so I must say thanks to Paul B (cheers for all the software you 'found' on the net), Harry for making even crappier jokes than me and always being at hand to help out, Moises for stories about meeting Che Guevara's mother, Chris B for his continual comical bitching and dodgy German accents, Diego for a smile that would melt the hearts of a 1000 Maltese whores, Simon M for being the only sane one in his group, Andy K for providing me with more samples than a man could ever desire, all the boys from footy for their silky smooth skills and, finally to Miss Ingrid Petri, who, through infinite generosity, let me run her car into the ground for a whole year.

However, this section would be wholly incomplete without thanking the one man without whom I wouldn't have had such a fantastic three years, a human of such standing that there aren't enough superlatives in the English language to fully do him justice, the mack-daddy, the daddy-mack, the bomb, the lick, the positron Sensai, the bees-knees, the big cheese, the anti-matter master, the master blaster, the king-pin, the crossword king, the man with the plan, Professor Paul G Coleman. You have had a hugely positive impact on my life Paul. Thank you my friend.

اپنی پیاری امّی ، پیارے ابّو

اپنے بھائیوں اور اپنی بہت پیاری بہن

کے لئے ، جن کی انتہائی محبت اور تعاون

سے ، الحمدُ للّٰہِ ، یہ کام انجام پایا ۔

Table of Contents

Chapter 1

Introduction

1.1 General

The massive leaps in the home PC processing power is but one example of the giant steps that the electronic-device fabrication industry has taken over the past few years. The reason for these advances is due to the indomitable drive towards further miniaturisation of electronic circuitry. Methods for achieving this, however, have several problems associated with them, e.g. altering of atomic structure, creation of defects in the lattice, and internal electric fields, which present the solid-state scientist with a wealth of atomic features to explore. There is not only interest from academia, but also from industry as to how the sub-atomic structure is affected by device-fabrication techniques. Therefore, an analysis technique that yields qualitative or quantitative information is not only desirable but also very necessary.

Ever since the discovery of the positron nearly 70 years ago [1], positron physicists have tried to exploit its unique behaviour in condensed matter. This has led to the emergence of a wide variety of techniques for investigating material structures, from the relatively inexpensive positron lifetime measurements [2] to depth-resolved measurements carried out using variable energy positron beams [3, 4, 5]. The principal reason for the burgeoning use of these techniques is due to the realisation that the positron-electron annihilation process depends almost entirely on the state of the positron-electron system in matter.

As well as the inexpensive nature of some positron-based techniques, another reason for the popularity of the positron in materials research is that it is a purely non-destructive probe, as the information is carried out of the system by penetrating annihilation radiation. Add to this the fact that no special sample preparation is necessary, and it becomes easy to see why it has become an attractive characterisation tool.

The advent of the intense, variable-energy positron beam opened the way for many new applications [6]. Whereas lifetime measurements and Doppler broadening spectroscopy only yielded information on the bulk of the material, tunable energy beams provided the user the option to study materials in the near surface region, typically up to depths of a few μm. This was a novel way of probing the sub-surface defected region of a material.

All the results of the positron annihilation experiments reported in this thesis have been carried out using the University of Bath (formerly University of East Anglia) slow positron beam. A full description of the beam and modification made to it can be found in chapter 3. The beam used is similar to several (what have now become standard) positron beams around the world. However, the work

done on the beam has tried to break away from the *standard* Doppler-broadening measurements, mainly by incorporating as-yet untried techniques for increasing the information obtained. These techniques include (a) improving depth resolution by progressive etch-and-measurement: (b) the first in-situ at-temperature defect annealing studies: (c) the first studies of laser-irradiated semiconductors : and (d) the application of Doppler broadening spectroscopy to ion implantation dosimetry.

The layout of the thesis is intended to allow the reader to gain readily an appreciation of the advances made. The present chapter gives a basic overview of positron physics. Chapter 2 discusses the principles of positron depth profiling as applied in solid-state physics, especially the positron's interaction with condensed matter. Chapter 3 presents a detailed description of the University of Bath positron beam and recent modifications made to it, as well as detailing some auxiliary non-positron techniques that were employed in aiding our understanding of the materials investigated. Chapters 4-8 describe specific examples of depth-profiling experiments. Chapter 4 deals with Doppler broadening measurements of boron implanted silicon coupled with the progressive etching of the sample in order to increase depth resolved sensitivity. Chapter 5 looks at a host of silicon samples implanted with various ions, at varying energies and at varying doses and tries to discern a pattern amongst them. Chapter 6 is concerned with an experiment involving the in-situ annealing of self-implanted silicon. Chapter 7 deals with laser-irradiated 4H-SiC.

1.2 Positrons

1.2.1 History

When Dirac predicted the existence of the positive electron in 1930 [1], he was taking a big step into the unknown. However, only three years later Anderson [7] proved him correct by discovering what is now known as the positron.

In the fifties, Deutsch demonstrated the existence of positronium [8] , the bound state of a positron and electron, and physicists spent the rest of the decade studying the properties of positrons and positronium atoms. From the sixties onwards, the positron was used for the study of condensed matter. Then, in the late seventies, Mills [9] was the first to successfully make the first positron *beam* using atomically-clean surfaces as moderators. The eighties saw a substantial growth in the number of slow-positron beams world-wide, producing monoenergetic positrons of energies from 1 eV to 50 keV.

1.2.2 Annihilation of Positrons

Positrons have the same mass (9.1095×10^{-31} kg) and spin ($\frac{1}{2}$) as electrons, but opposite charge and magnetic moment. They are stable in vacuum (lifetime at least 2×10^{21} years) but rapidly thermalise and annihilate with electrons in materials, predominantly via 2γ decay (of energy approximately 511 keV) with a mean lifetime of typically only a few hundred picoseconds.

When the positron and electron wave-functions overlap, the particles annihilate,

emitting photons. In dense materials this annihilation process takes place predominantly via two photon annihilation:

$$e^+(\uparrow) + e^-(\downarrow) \longrightarrow 2\gamma \tag{1.1}$$

When both the positron and electron are at rest at the moment of annihilation, the conservation of momentum causes the two γ photons be emitted collinearly in opposite directions, each with an energy of $m_e c^2 = 511$ keV.

If the total momentum of the annihilation particles relative to the laboratory frame is non-zero, the γ photons are emitted anti-collinearly in the centre of mass frame of the electron-positron pair. However, in the laboratory frame the γ momenta are no longer at 180^0. For non-relativistic electrons and positrons ($p \ll m_e c$) the energy of the 511 kev γ quanta observed in the laboratory frame are given by

$$m_e c^2 \pm \triangle E \tag{1.2}$$

The broadening, $\triangle E$, of the 511 keV annihilation line can be calculated from the electron momentum component in the propagation direction, p_z:

$$\triangle E = \frac{p_z c}{2} \tag{1.3}$$

A typical value of the momentum of electrons in metals based on the free elec-

tron model is 1.5×10^{-24} kgms^{-1}, corresponding to $\triangle E$ of 1.4 keV which is approximately the resolution of modern solid-state detectors.

Experimental Techniques

Positron experimental techniques fall broadly into 2 categories, depending on whether they give information on the *annihilation rate* of the positrons or on the *momentum distribution* of the annihilating positron-electron pair.

1.Annihilation rate: The annihilation rate, λ, is given by the overlap of the positron and electron densities at the annihilation sites [10]. The positron lifetime is the inverse of the annihilation rate:

$$\tau = \lambda^{-1} \tag{1.4}$$

When a positron is trapped in an open-volume defect, such as a vacancy, the lifetime increases with respect to the defect-free (bulk) sample. This is due to the locally reduced electron density of the defect. Generally, the shorter the positron lifetime, the higher the electron density at the site of the annihilation.

2.Momentum distribution: At the point of the electron-positron annihilation, the positron has fully thermalised and its contribution to the Doppler broadening of the annihilation γ can be taken as zero. Therefore, the annihilation photons carry information about the local momentum distribution of the electrons in the specimen, namely p_z. This forms the heart of the Doppler broadening technique and is the principal technique used to obtain measurements for this thesis.

1.2.3 Positronium formation and annihilation

It is possible under some circumstances for a positron to bond with an electron to form a positronium (Ps) atom with a vacuum binding energy of about 6.8eV.

The spins of the particles ($s_+ = s_- = \frac{1}{2}$) gives rise to two possible states.

(i) Spins aligned so that the total spin $s = s_+ + s_- = 1$. This is the triplet state, orthopositronium (o-Ps).

(ii) Spins anti-parallel so that $s = s_+ - s_- = 0$, giving the singlet state, para-positronium (p-Ps). The lifetime of p-Ps in vacuum is 125 ps, whilst that of o-Ps is 142ns, which principally decays via 3 γ annihilation [11]. In most materials with a high electron density the lifetime of o-Ps will be reduced to a few nanoseconds because the o-Ps annihilates via a *pickoff*-reaction, in which the positron annihilates a bulk electron, or by quenching, in which the parallel-spin electron is exchanged for an electron with anti-parallel spin, both enabling 2 γ annihilation.

Ps may also be formed by the ionisation of valence electrons by the energetic positrons and subsequent bonding to this electron (Ore mechanism) or by the positron capturing an electron during slowing down (Spur mechanism). The formation of Ps in the bulk of most materials with high electron density e.g metals and semi-conductors, is not possible due to the size of the positronium atom (the same as hydrogen) and electron screening. However, in material with small voids, it is possible.

Chapter 2

Positron Depth Profiling

2.1 Introduction

Over the past two decades, positrons have proved to be a powerful tool for the depth profiling of a host of materials, some of which include ion-beam modified materials, epitaxially-deposited layers on semi-conductors and more general deposition of thin films and coatings [3].

Positrons have a natural affinity with sites in a material where no ion cores are present, meaning they are sensitive probes for open volume defects. As well as trapping and annihilating in defects, other positron processes can occur: trapping at surfaces, positronium formation at surfaces, positronium desorption and 'free' annihilation in undefected material. It is possible to derive this information from annihilation measurements so that not only do we obtain information on the annihilation site, but also on the positron diffusion behaviour and branching at

the surface. Since the positron is a charged particle its diffusive motion will be influenced by the presence of internal electric fields. This chapter briefly summarises positron interactions in solids, as well as showing how to extract information from positron experiments.

2.2 Positron Interaction with Matter

2.2.1 Implantation

When an energetic positron is implanted into a solid, it can have several fates. Apart from a fraction that backscatter at the surface, the positron undergoes several energy loss mechanisms before it is finally thermalised.

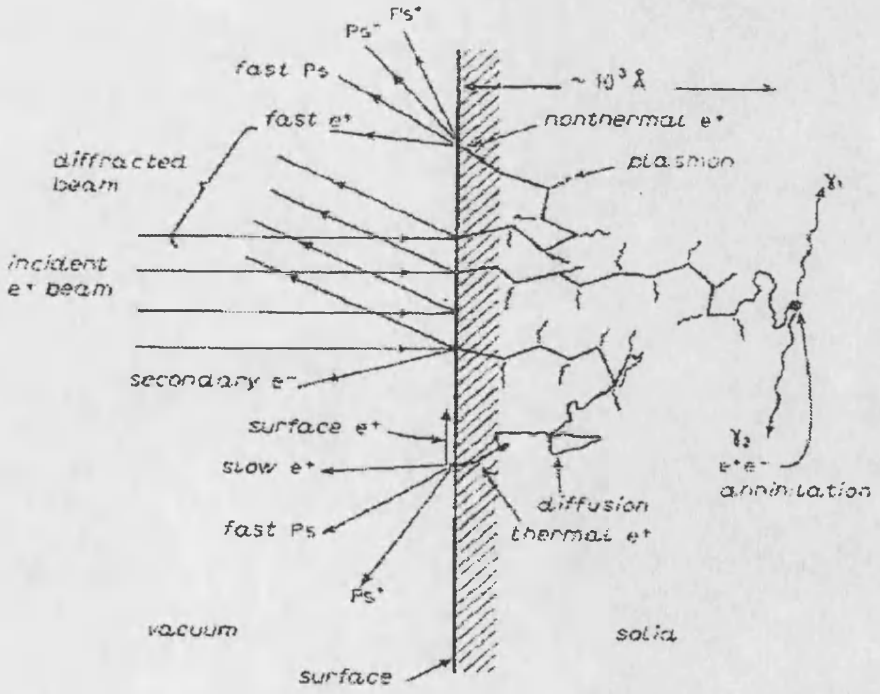

Figure 2.1: Possible fates of energetic positrons entering a solid[12].

The positron's fate can be sectioned into three categories. Firstly, the positron may remain in a Bloch (delocalised) state and diffuse around until it annihilates with an electron in the material when their corresponding wave-functions overlap. Secondly, the positron may trap in a defect and annihilate. There is also the possibility that it may de-trap, this having been known to occur in shallow traps. Thirdly, the positron may diffuse back to the surface. Here it can: be reflected back into the material by the surface potential, trap in a two-dimensional surface state or near-surface defect [13], or be emitted, either as a free positron or pick up an electron on the way out and form positronium. The various possibilities are represented diagrammatically in figure 2.1.

Positrons implanted close to the surface may return to the outer surface before being fully thermalised [14] leading to the emission of epithermal positrons and 'hot' positronium.

2.2.2 Stopping, Slowing down and Thermalisation

The kinetic energy of an implanted positron exceeds the thermal energy k_BT considerably. The difference between these two energies is dissipated in the crystal due to a variety of lattice interactions (scattering, electron/phonon excitation etc.). This process is known as thermalisation and typically occurs within the first picosecond, a much shorter duration than the positron lifetime($\sim 10^2 ps$).

At very high positron energy (MeV domain), the positrons are mainly thermalised by their interaction with the screened Coulomb field of the nucleus or one of the atomic orbital electrons. Below 100 keV, the primary energy loss mechanism is by electron scattering with most of the positron's kinetic energy lost through

core and valence electron excitations. Through these interactions, the energy is reduced to a few electronvolts within a picosecond. It is now that the contribution of phonon scattering to the stopping process becomes more dominant. Phonon excitations have a much lower energy transfer rate than electron interactions so the phonon stopping times are therefore much longer than the electron ones. While the time to slow down a positron to near-thermal energies amounts to less than a picosecond, phono stopping times (for complete thermalisation of the positron) are of the order of 10 ps [15].

2.2.3 The Implantation Profile

Being a light particle, an energetic positron may thermalise at a wide range of depths below the surface, described by the implantation profile. This profile has been investigated experimentally (via thin film penetration) and theoretically (via Monte Carlo simulation). The profile can be parameterised by the Makhovian function [16]:

$$P(E,z) = \frac{mz^{m-1}}{{z_o}^m} exp\left[-\left(\frac{z}{z_o}\right)^m\right] \tag{2.1}$$

where $P(E,z)dz$ is defined as the fraction of positrons entering a solid with initial energy E that will be stopped at a depth between z and $z+dz$.

The parameter z_0 is 1.2 $\times$ the mean implantation depth of a positron implanted with energy E and is given by:

$$z_0 = \frac{\alpha}{\rho} E^n \tag{2.2}$$

where ρ is the density of the material (gcm^{-3}). There has been a great deal of discussion as to what value to assign to the constants m, n and α. The values assigned to them can influence the analysis of experiments which use positrons returning to the surface as their basis, as knowing the shape of $P(E,z)dz$ within a diffusion length of the surface is important. However, for the analysis of Doppler broadening measurements, the model is concerned with the number of positrons annihilating in a slice of thickness Δz below the surface and the actual form of $P(E,z)$ is not as critical [17], as long as the correct z_0 is used. Therefore, the values used are the generally accepted ones of $m = 2.0$, $n = 1.6$ *and* $\alpha = 4.0$ $\mu\mathrm{gcm}^{-2}$.

2.2.4 Diffusion

After implantation and thermalisation, the positron diffuses through the material. For analytical purposes, the positron may be considered analogous to a hole in a semiconductor. Its *diffusivity* D_+, and mobility μ, are related by the Einstein equation:

$$eD_+ = k_B T \mu \tag{2.3}$$

where k_B is Boltzmann's constant (1.3×10^{-23} JK^{-1}) and e is the elementary charge (1.60×10^{-19} C). The positron diffusivity can relate to the probability

that a thermalised positron reaches a trap.

The positron diffusion length, L_+ during its bulk lifetime τ_b in a defect-free material is:

$$L_+ = \sqrt{D_+ \tau_b} = \sqrt{D_+ / \lambda_b} \tag{2.4}$$

where λ_b is the positron annihilation rate. A typical room temperature measurements of D_+ in silicon is 2.7×10^{-4} m^2 s^{-1} [18] while the lifetime is 218 ps [19]. This yields $L_+ = 243 \pm 10$ nm in silicon, which is small in comparison to the implantation depth.

2.2.5 Trapping

If there is an open-volume defect in a lattice, the positron wave-function can condense into the potential minimum with high efficiency [20]. In materials with a uniform defect distribution, trapping of the positron reduces the diffusion length to an effective diffusion length $L_{+_{eff}}$:

$$L_{+_{eff}} = \sqrt{\frac{D_+}{\lambda_b + \kappa_t}} \tag{2.5}$$

where κ_t is the trapping rate into defects, given by:

$$\kappa_t = \nu_t C_d \tag{2.6}$$

ν_t represents a specific trapping rate for a certain defect that is present in the lattice with atomic density C_d.

2.2.6 Work function

The positron work function ϕ_+ is defined as the minimum amount of energy required to move a positron from a point inside a material to one at an infinite distance from the surface and is given by:

$$\phi_+ = -D - \mu_+ \tag{2.7}$$

where μ_+ is the (bulk) positron chemical potential and D represents the surface dipole barrier which is primarily caused by the tailing of the electron distribution into the vacuum.

Positrons experience the force of the dipole barrier in a direction out of the solid, which, because it opposes that attractive image-correlation potential, causes ϕ_+ to be nearly zero, and, in the case of a clean tungsten surface, even negative, allowing the emission of slow positrons into the vacuum [21].

2.2.7 Annihilation and the S-parameter

As mentioned previously the extent of the Doppler broadening about the 511 keV annihilation energy is typically a few hundred electronvolts.

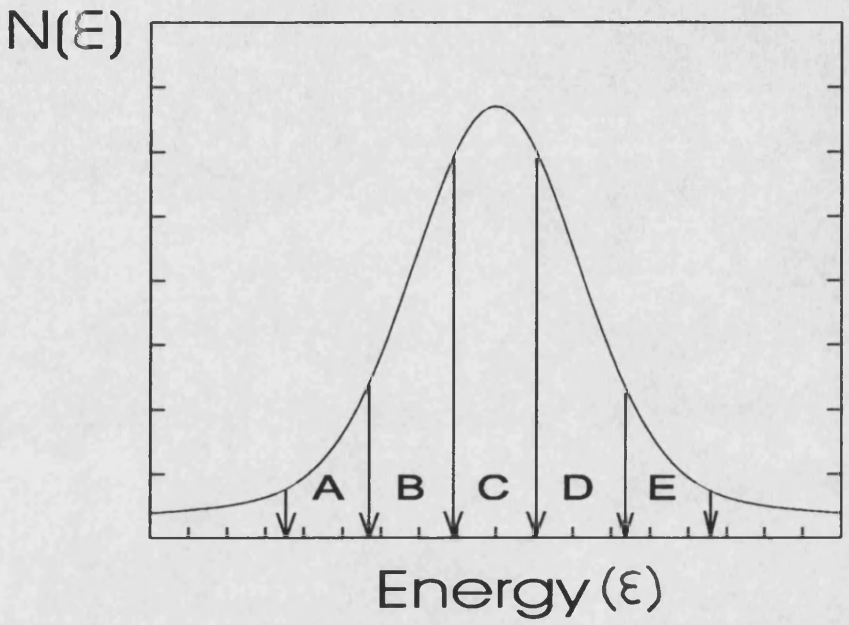

Figure 2.2: Regions chosen for determining S and W

Figure 2.2 shows a schematic of the photopeak of a gamma ray energy spectrum produced by a Ge detector centred on 511 keV. The extent of the broadening is characterised by specific line parameters, namely the so called S (*Sharpness*) parameter [22] defined as:

$$S = \frac{C}{A+B+C+D+E} \tag{2.8}$$

where A to E represents the areas of the peak sections shown in figure 2.2 and which gives information about the low-momentum part of the peak. The W (*Wing*) parameter given by:

$$W = \frac{A+E}{A+B+C+D+E} \tag{2.9}$$

which pertains to the high momentum region. The interval limits are chosen symmetrically about 511 keV, and picked so as to obtain the maximum statistical precision, which in practice translates as $S \sim 0.5$ [23] and $W \sim 0.25$ measured in a defect-free material.

It should be noted that the absolute value of S carries no direct physical information due to its dependence on the photon-detection system. However, a normalised S-parameter, defined as

$$S_{norm} = S/S_{bulk} \tag{2.10}$$

where S_{bulk} is the value of S in a defect free sample can be used for comparing Doppler broadening measurements between different laboratories. Caution should still be exercised, however, as it has been shown that S_{norm} may also be system dependent [24].

Relating S to material properties

The S-parameter is a measure of the average momentum available in the positron-annihilation process. Free (delocalised) positrons are able to annihilate with both core and conduction electrons, whereas positrons trapped in vacancies are less likely to annihilate with core electrons due the small overlap of their wave function resulting from the absence of the ion core in the defect. Therefore, trapped

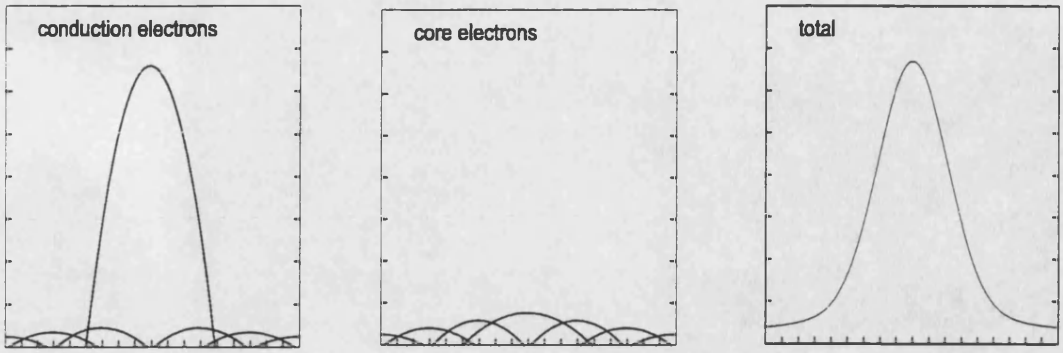

Figure 2.3: Conduction and core electron contributions to 511 keV photopeak. Axes are as in figure 2.2.

positrons have a greater probability of annihilating with conduction (lower momentum) electrons than free positrons, which can annihilate with core (higher momentum) electrons. This is shown schematically in figure 2.3.

When viewed in terms of the extent of broadening of the photopeak, annihilations with conduction electrons will produce a narrower peak and, consequently, a higher S-value, whereas annihilations with core electrons will lead to a broader peak and a lower S-parameter. Therefore, generally speaking, a high S-value indicates that positrons mainly trap in vacancies and a low S indicates that a large fraction annihilate in the bulk.

For the S-parameter to be useful, it needs to relay more quantitative information on the system. For each positron implanted with energy E, the S-parameter can be written as:

$$S(E) = f_s(E)S_s + f_b(E)S_b + f_d(E)S_d \tag{2.11}$$

where $f_s(E)$, $f_b(E)$ and $f_d(E)$ denote the energy dependent fractions of positrons annihilating at the surface, in the bulk or at a defect with specific S_s, S_b and S_d values. There may not be only one type of defect in a material, meaning that the defected region has to split up into i slices, each with an $S_{d,i}$ value. Now, for f_b and f_d are related to each other by:

$$\frac{f_b}{\sum_{i=1}^{n} f_{d,i}} = \frac{\lambda_b}{\sum_{i=1}^{n} \kappa_{d,i}} \tag{2.12}$$

where $\kappa_{d,i}$ is the positron trapping rate for defects in slice i (see equation 2.6).

Equation 2.11 shows that the S-parameter carries information about the defects at which the positron annihilates. Defects with a high trapping rate or with a high concentration (see equation 2.6) may influence the annihilation-peak width considerably.

Statistical Error in S

The statistical error σ_s in Doppler S-parameter measurements is estimated from a binomial distribution [25]:

$$\sigma_s = \sqrt{\frac{S(1-S)}{N}} \tag{2.13}$$

where S is the measured S-parameter and N represents the total number of counts in the 511 keV peak. To minimise the error in S, $\frac{d\sigma}{dS} = 0$, giving $S = \frac{1}{2}$. As typical variations in measured S are of the order of one percent, the total number of counts collated in an average S-parameter measurement is about 1×10^6.

2.2.8 Epithermal effects

Positrons that have not been fully thermalised and that are ejected from the material are known as epithermal positrons. In material with inefficient stopping mechanisms at near-thermal energies (insulators, semiconductors), the number of re-emitted positrons is not negligible and must be taken into consideration. One option is to ignore the lower positron energy data, as these points are more susceptible to epithermal effects. Another solution is one employed in the fitting program VEPFIT (see section 3.4.3) where an epithermal scattering length is introduced in order to estimate the number of positrons returning to the sample surface, annihilation of which yields a separate S-parameter.

2.2.9 Positronium Detection

As described previously, it is possible for a positron to bind with an electron to form a positronium (Ps) atom, either in the triplet state, ortho-Ps, or the singlet state, para-Ps. Since ortho-Ps decays primarily into three γ-rays of total energy $\sim 2mc^2$, the resultant γ-spectrum has a continuous energy distribution ranging from 0 to $\sim mc^2$. The annihilation spectrum recorded in the presence of ortho-Ps decay will be markedly different from the usual two-photon annihilation or

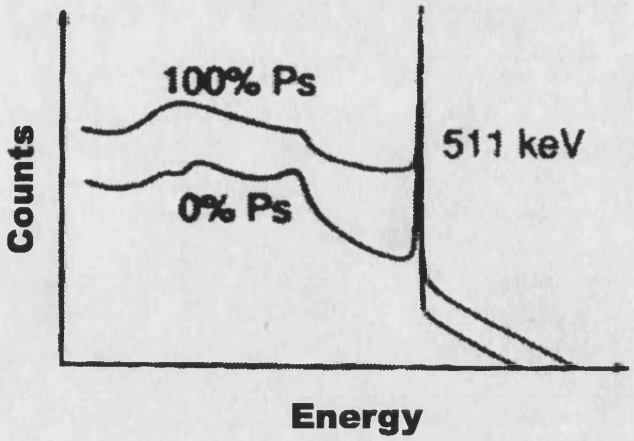

Figure 2.4: Positronium fraction, the fraction of positrons that form positronium. The plot shows two extreme case of 0% and 100% Ps formation.

para-Ps decay. Figure 2.4 shows a typical spectrum, with a 'peak' region centred on 511 keV, comprising of counts from para-Ps decay and, a 'valley' region to the left of the peak, resulting from ortho-Ps decays. The graph shows the two extreme cases of 0% and 100% Ps formation. By taking a ratio of the valley to the peak counts, one can determine the Ps fraction in relation to the two 0% and 100% extremes.

Chapter 3

University of Bath Positron Beam and Auxiliary Techniques

3.1 Introduction

The first part of this chapter is concerned with the workings of the University of Bath positron beam, and modifications made to it over the past few years. This includes not only the positron transport system, but the electronics used for collating the data and the various software programmes used for analysis of the measured spectra.

The latter part of the chapter looks at some auxiliary techniques that have been used to aid in the understanding of the materials being investigated.

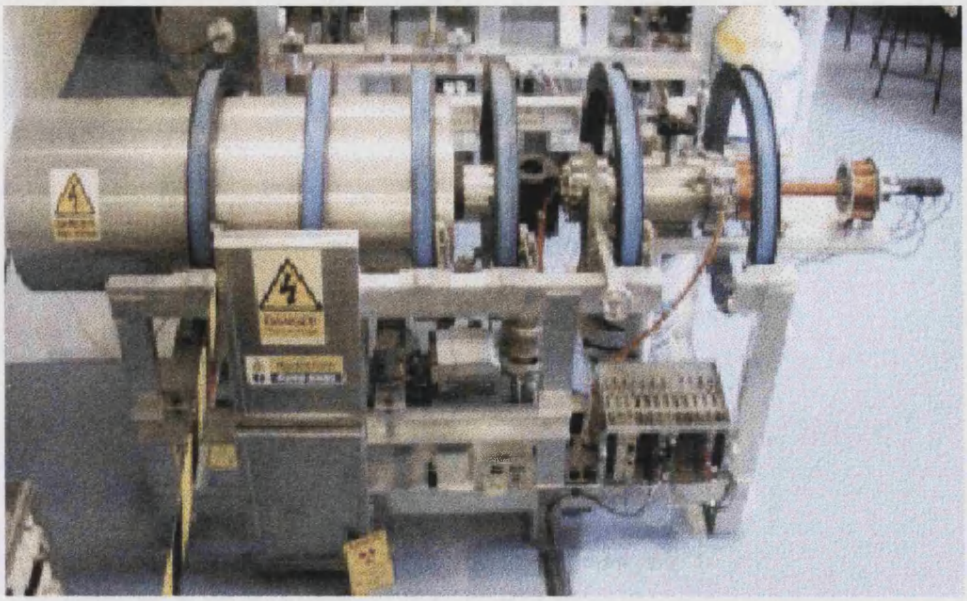

Figure 3.1: Photograph of the University of Bath slow positron beam

3.2 The Beam

3.2.1 General Description

The slow positron beam used at the University of Bath for the experiments detailed in this thesis is shown in figure 3.1 and is represented schematically in figure 3.2. The whole framework of the set-up is constructed of non-magnetic material. The coils are supported by this framework in such a way that they can be adjusted if the beam needs correcting. The positron source (**D**) is a ^{22}Na β^+ emitter which sits behind an annealed W mesh moderator. The moderated positrons traverse towards the sample end, through a vacuum of $\sim 10^{-6}$ torr, pumped down initially by a rotary pump and then a turbo pump (**K**). The beam is guided down the axis of the apparatus by a set of six Helmholtz coils (**C**) towards the sample chamber (**M**), where the positrons annihilate. Decays are detected by a Ge crystal detector, the scintillations being recorded on a Multi-Channel Analyser (MCA) and read by computer software.

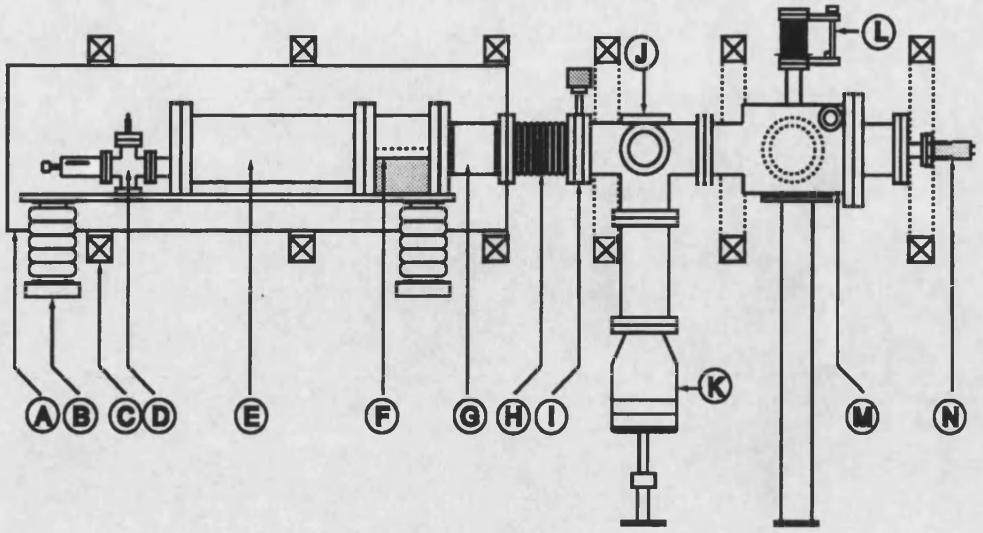

Figure 3.2: Schematic of magnetic–transport beam system. A–grounded shield: B–standoff insulators: C–coils for magnetic field: D–source/moderator: E–$\underline{E} \times \underline{B}$ plates: F–lead-shielding: G–accelerator: H–bellows: I–gate valve: J–guiding coils: K–turbo-pump: L–sample manipulator: M–sample chamber: N–CEMA/CCD camera

3.2.2 Positron Source and Moderator

The positron source used is a ^{22}Na β^+ emitter with $\tau_{\frac{1}{2}} \sim 2.6$ years and which had an initial activity of 20 mCi (660 MBq). Positrons are emitted from the source with a continuous energy spectrum, of mean energy $\sim$ 200keV, which would implant themselves to depth of 0.1 mm in a given material, making them unsuitable for near-surface studies. For the positrons to be of practical use in controlled defect-depth profiling, they need to be moderated to a few eV. This is achieved by placing a 7 μm thick 99.95% pure polycrystalline tungsten mesh in front of the source in transmission-moderation geometry. The tungsten has a negative positron work-function (see section 2.2.6), with an efficiency of 4×10^{-4} slow positrons emitted per β^+ reaching it. The tungsten is at a potential 10V less than the source so that positrons re-emitted in the backwards direction are pushed back into the forward direction, and is annealed regularly to maintain its efficiency.

3.2.3 Velocity Filtering

On passing through the tungsten moderator, the beam will comprise of moderated slow positrons and some fast positrons that have managed to pass through the mesh. In order to filter these unwanted fast positrons out, the beam passes through two parallel Wien [26] $\underline{E} \times \underline{B}$ plates (**E**) which produce an electrostatic field perpendicular to the axial field and deflects the fast positrons out of the beam.

3.2.4 Magnetic Transport System

The beam is transported by a solenoidal magnetic field provided by a set of six copper-wound coils which produce a uniform axial field of 0.01T (100 gauss) that is large enough to confine a positron with transverse kinetic energy 1eV to a gyration radius of 0.25mm.

The positrons are accelerated by a set of 10 smooth metal discs, separated by 40MΩ resistors, with 2 inch holes in the centre (**G**), across which a potential gradient of up to 30 keV is applied.

3.2.5 Beam Alignment

At the end of the beam is a Channel Electron Multiplier Array (CEMA), across which 2 kV is applied. Behind the CEMA is a phosphor screen, held at +2 kV with respect to the back face of the detector. A small CCD video camera (**N**)

is attached to the window on the CEMA, enabling one to see the positrons as they cause the phosphor screen to fluoresce when they are incident upon it. By watching the beam's shadow whilst moving it transversely to its axis (using a pair of guiding coils (J) placed perpendicularly to the axis of the beam), it is possible to position the beam at a desired position.

When the positrons impinge upon the sample, the annihilation gammas are detected by pure Ge crystal detector (see section 3.4.1).

3.3 Beam Modifications

3.3.1 Decreasing Sample turnaround time

In the past, whenever it has been necessary to change the sample being measured, the whole of the vacuum system had to be let up to atmosphere pressure, the sample changed, the system re-pumped and the tungsten moderator re-annealed. This was a laborious and time-consuming process. By placing a gate valve between the sample chamber and the turbo-pump (I in figure 3.2), the possibility of being able to let up to air only the sample chamber was viable. A rotary pump was placed on an inlet at the sample end, allowing a coarse vacuum of $\sim 10^{-2}$ Torr to be attained before opening of the valve. As a result of keeping the source end at vacuum, the life of the moderator has been lengthened due to it having to be annealed less frequently.

3.3.2 In-situ annealing

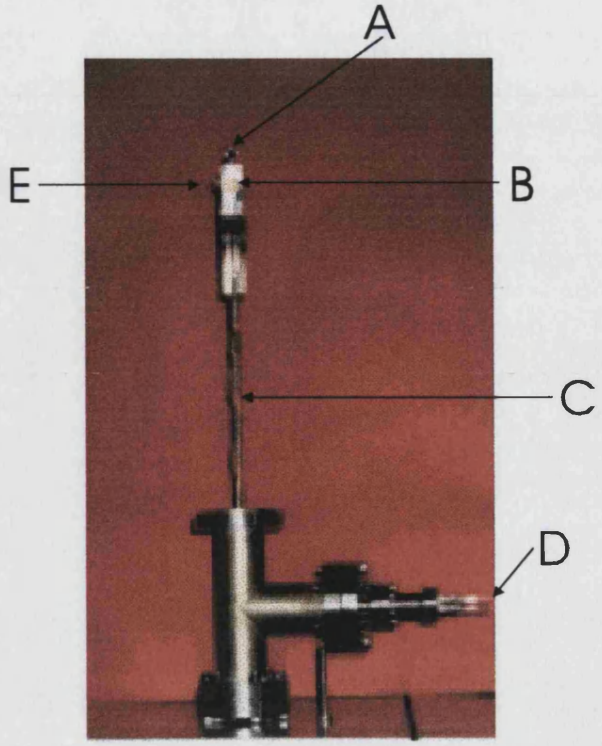

Figure 3.3: Heating device built for in-situ annealing. A–Positioning target: B–Sample: C–Threaded Post: D–Thermocouple and heater connections: E–Thermocouple junction

An important aspect of studying defect profiles is to investigate defect behaviour at varying temperature. Figure 3.3 shows the heating system that was designed and constructed for taking measurements in an in-situ environment (see chapter 6). The main head of the device is based on a second-generation combined sample holder and electron beam heater designed by A. Goodyear [27]. The sample stage of the heater is electrically isolated from the heater unit enabling high voltages to be applied to the sample when required. A chromel-alumel thermocouple junction (**E**)is sandwiched between the sample (**B**) and a cover plate. The heater and thermocouple wires run along the threaded post(**C**) to the high voltage connection points (**D**). These are attached to an electron beam power supply with Eurotherm temperature controller on which the temperature required may be set. The power supply has an in-built self-tuning feedback function that corrects

the actual temperature of the sample to that set on the controller. This does, however, take time to respond, and the sample temperature tends to overshoot the set value; the sample temperature has thus to be raised slowly and carefully. The purpose of the diamond shape protruding at the base of the device (**A**) is to aid in the positioning of the beam onto the sample. The shadow of the reference target can be seen on the CCD camera allowing for beam alignment at varying energies. Once accomplished, the sample holder is lowered so that the beam now impinges directly onto the sample.

3.3.3 Low-Temperature Measurements

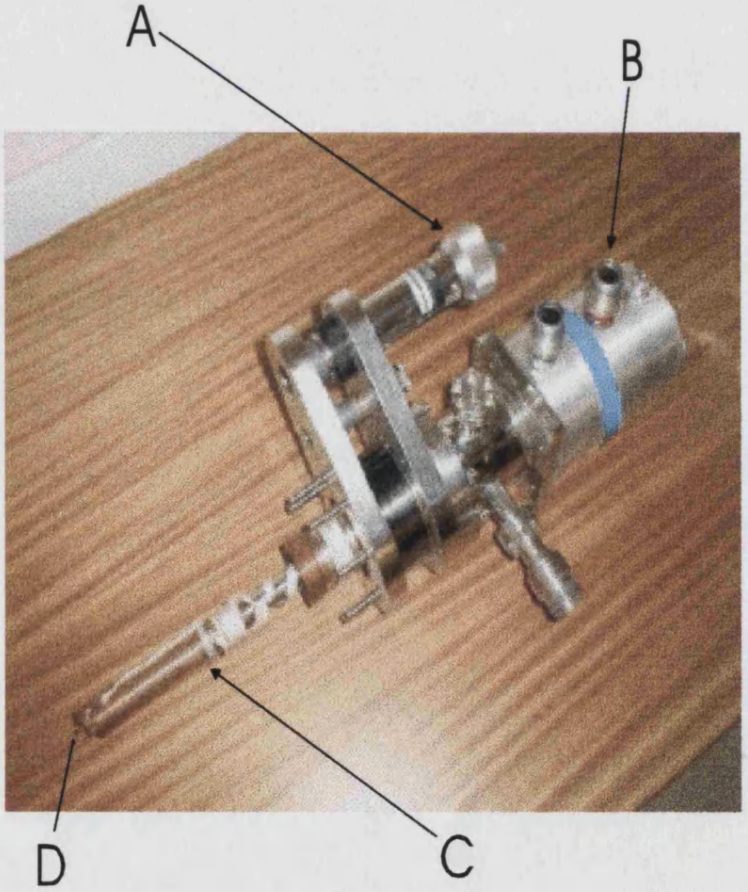

Figure 3.4: Cold finger arrangement for low temperature measurements. A–Horizontal translator: B–APD cryogenic pump: C–Sample holding copper rod: D–Positioning target

From time to time, it is necessary to make S-parameter measurements on samples at low temperatures e.g. on superconductors. Figure 3.4 shows the setup that was built for such a purpose. The setup comprised of a Displex [28] closed-cycle refrigeration system (**B**) attached to a horizontal translator (**A**) with an extended conducting copper rod (**C**). The sample is glued to a flat section on the rod, and this is placed such that it intersects the beam by using the diamond at the end of the rod (**D**) as a positioning tool. It was necessary to remove the sample chamber (**M** in figure 3.2) and replace it with a cross-piece so that the cold-finger arrangement could enter from the side of the system, and not from above as before. It was therefore possible to move from the positioning-diamond to the sample using the horizontal translator.

3.4 Data Acquisition and Analysis

Once the positrons have been successfully moderated, accelerated and guided to the sample, they implant themselves into the sample and annihilate. In order to extract some useful information from the annihilation gammas, several steps need to be taken.

3.4.1 Electronics

Figure 3.5 shows a schematic for the electronics setup used for the measurements outlined in this thesis. The annihilation gammas enter a Ge crystal detector [29], which is cooled by liquid nitrogen (to reduce thermal noise). Gamma rays which lose all their energy via the photoelectric effect will cause the crystal to electron-

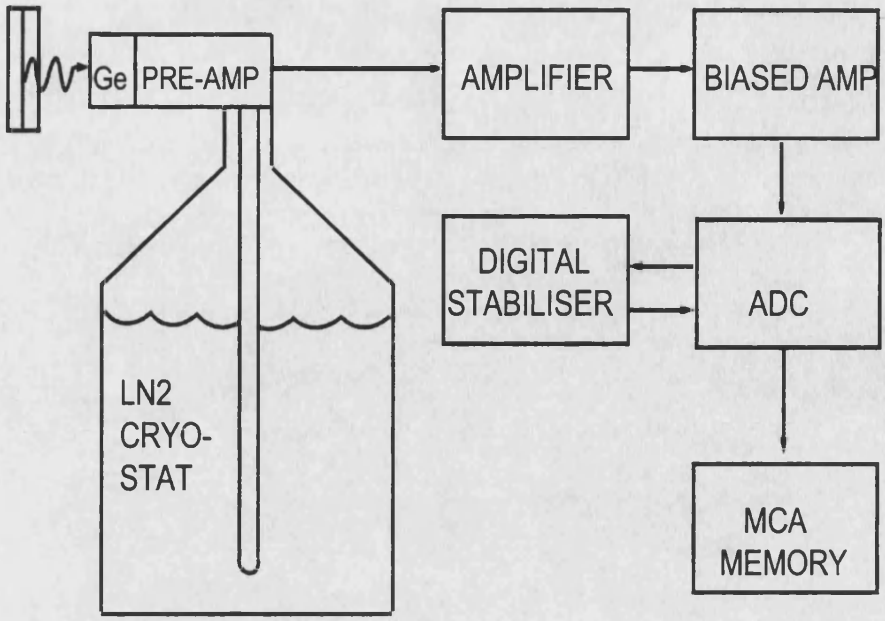

Figure 3.5: Schematic of the electronics setup used for positron measurements

avalanche, with the resultant voltage peak being proportional to the energy of the original gamma.

The analogue voltage is the amplified to a value between 0 and 10V by an amplifier [30]. The signal is then biased [31](to concentrate on the relevant part of the spectrum - the photopeak) before being passed into an ADC[32] (Analogue-to-Digital-Converter) connected to a digital stabiliser [33] (to compensate for temperature and other shifts in the amplification stages). The digitised pulses are then sent to an MCA (Multi-Channel Analyser) board inserted in a computer (see section 3.4.2).

3.4.2 CONTROL software

During the time that the work in this thesis has been carried out, the positron beam has been controlled by two generations of software. Both versions have

broadly similar properties, so the following description is relevant for either.

The CONTROL software for manipulating the beam is run on a Pentium class PC. The software allows the user to manipulate the beam energy and position by varying the output voltages on a six channel Digital to Analogue converter board [34] that is inserted on the motherboard of the PC. The outputs from the card interface with analogue control input lines on the power supply and with a set of perpendicularly-placed coils situated halfway down the beam line, which counter the effects of beam movement about its axis at different accelerating voltages.

There is also a Multichannel Analyser (MCA) board [35] installed in one of the expansion slots. An MCA stores the number of counts from the detector which fall in discrete energy steps and displays these finely binned data as a histogram. The board takes these data from the germanium detector and uses the memory on the board itself to store the counts per channel data. The MCA can be accessed by the control software, running for a predetermined time, making necessary calculations, and storing the data ready for plotting.

3.4.3 Fitting of data

After having obtained the data output file given by the control program, it must be interpreted properly to identify various features of possible multilayer systems or with different types of defect. There are two programs which fit S-parameter profiles in broadly similar fashions that have been used to analyse the data contained in this thesis, these being VEPFIT [36] and POSTRAP [37].

For a positron probability density $n(z)$, all processes to which thermal positrons

are subjected can be combined in a single equation, the one-dimensional, steady-state positron diffusion equation for the positron number density $n(z)$:

$$\frac{d^2n(z)}{dz^2} - \frac{d}{dz}\left[\frac{n(z)}{\Lambda(z)}\right] - \frac{n(z)}{L^2} + \frac{n_0(z)}{D_+} = 0 \tag{3.1}$$

where in addition to earlier defined symbols (see section 2.2.4), $\Lambda = k_BT/e\xi$ is a parameter with the dimensions of length which characterises the electric field $\xi(z)$. In principle, the position-dependent values of the positron diffusion length are given by

$$L \equiv \sqrt{D_+\tau_{eff}} = \left(\frac{D_+\tau_{bulk}}{1+\mu C_d\tau_{bulk}}\right)^{\frac{1}{2}} \tag{3.2}$$

which shows that $L(z)$ is a primary source of information about the defect concentration profile $C_d(z)$ in the system.

Often, an inhomogeneous system is treated as a series of homogeneous slabs for numerical analysis. Each slab j is treated as homogeneous with constant values of diffusion length L_j, and electric field ξ_j, with the diffusion equation (equation 3.2) yielding energy dependent fraction $F_j(E)$ of positrons annihilating in each slab. The predicted value of the lineshape parameter S is given by (the more general form of equation 2.11):

$$S(E) = \sum_{\text{layers}_j} F_j(E)S_j \tag{3.3}$$

where S_j is the lineshape parameter characteristic of layer j. Both VEPFIT and POSTRAP find a set of slab parameters L_j, ξ_j, S_j etc, that give an optimum fit to the experimental data. They vary in the way in which the data is entered in the input file. POSTRAP allows one to specify j defect regions, each of a certain depth and defect concentration, whereas VEPFIT asks for a value of the diffusion length in each. It is possible to obtain a fitted defect concentration from both programs in accordance with experimental data.

3.5 Auxiliary Techniques

Most of the samples used for work detailed in this thesis were fabricated either at, or in collaboration with, the University of Surrey. It seems, necessary, therefore, to give a brief overview of the ion-implanter used for fabricating the samples investigated, as well as looking at some auxiliary techniques used to complement the positron method.

3.5.1 Danfysik Ion Implanter

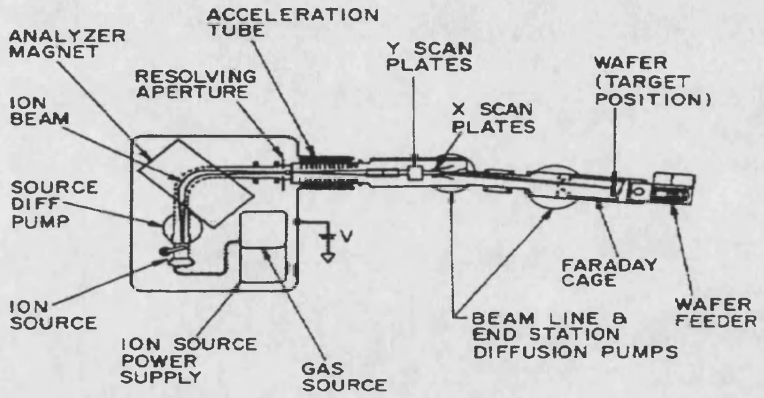

Figure 3.6: Schematic of a typical commercial ion-implantation machine.

Figure 3.6 shows a schematic diagram of an ion-implanter, similar to the one used at the University of Surrey. The gas source feeds a small quantity of gas into the ion source where a heated filament causes the molecules to break up into charged fragments. An extraction voltage of around 30kV causes the ions to move out of the ion source into the analyser. The pressure is kept below 10^{-6} Torr to minimise scattering by gas molecules. The magnetic field of the analyser is chosen such that only ions with the desired charge to mass ratio can travel through without being blocked by the analyser wall. Surviving ions continue

to the acceleration tube, where they are accelerated to the implantation energy (from $10^3 - 10^6$ eV) as they move from high voltage to ground. Apertures ensure that the beam is well collimated. The beam is scanned over the surface of the wafer using electrostatic deflection plates. The wafer is offset slightly from the axis of the acceleration tube so that ions neutralised during their travel will not be deflected onto the wafer. A commercial ion implanter is typically 6m long, 3m wide and 2m high, consumes 45kW of power and can process 200 wafers per hour.

3.5.2 Secondary Ion Mass Spectroscopy (SIMS)

SIMS measurements provide a way of measuring the chemical composition of a near surface region of a material. A primary ion beam with a typical energy of between 1 and 10 keV is incident on a surface. Due to the transferred impact energy neutral atoms, molecules and ions - so called *secondary ions* - are emitted from the surface whence they are analysed and detected by a mass spectrometer The measured mass spectrum then yields information about the chemical elements and their depth distribution in the near surface region.

Chapter 4

Low Energy Boron Implanted Si

4.1 Introduction

Ion implantation has been used in Si MOS integrated circuit fabrication since the early to mid-1970s for the purpose of forming doping profiles required in MOS transistors and memory cells. Its advantages over other doping methods include accurate dose control, higher purity of the dopant species, reproducibility of the impurity profiles, the ability to selectively dope the silicon and the ability to tailor the doping profile.

However, as device dimensions decrease, scaling of the doping parameters must occur concurrently in order to maintain adequate device electrical characteristics. Process modelling and control of dopant profiles on these new length scales require greater understanding of implantation profiles and defect production than ever before. The implantation process creates lattice vacancies, a few percent of

which survive the initial migration and annihilation with interstitials and either coalesce into divacancies [38] or form room temperature impurity-defect complexes [39]. This concentration of open-volume defects can affect the performance of the devices, and it is thus important to gain as much information about them as possible.

Positrons have shown themselves to be a useful ally to the Si integrated technology industry, providing them with a novel and non-destructive means of supplying quantitative information on the defect profiles caused by the ion-implantation process. They have been shown to probe depths of $\sim 10^2$ to 10^3 nm, as well as showing sensitivity to defects at concentrations as low as 10^{-7} per atom[40].

The computer code TRIM [41] is widely used in the microelectronics industry to predict both ion and vacancy depth profiles following ion implantation. TRIM does not allow for the effects of ion channelling and/or post-implantation diffusion on either distribution. Additionally, the loss of vacancies referred to earlier is not accounted for. The dopant distribution can be determined experimentally via depth profiling using secondary ion mass spectroscopy (SIMS). Positron Annihilation Spectroscopy (PAS) offers the ability to yield information beyond - sometimes by a considerable factor - those predicted by TRIM [42, 43].

Due to the drive to implant at lower energies and fluences, broadening of the ion profile following post-implantation annealing is becoming increasingly significant. For such shallow implantation, the final dopant profile is strongly affected by the implant induced damage due to defect enhanced diffusion [44].

In this chapter results are presented of PAS measurements of structural damage resulting from the implantation of 5 keV B^+ ions into FZ-(float-zone) Si at

fluences as low as 2×10^{12} cm^{-2}. Because the positron implantation profile becomes increasingly extended as the incident positron energy (and hence mean implantation depth) increases, the depth sensitivity of the technique decreases with depth. Furthermore, the fact that the majority of positrons annihilate in vacancies in the large peak just below the surface means that the ability of PAS to study lower-intensity extended vacancy-type defect tails is limited. To increase the sensitivity, the standard non-destructive PAS technique was combined with etching of known sample thickness, extending the idea of Fujinani and Chilton [43] by controlling the etching process via anodic etching.

4.2 Experimental Details

4.2.1 Sample Preparation

Four FZ-Si samples were implanted with 5keV $^{11}B^{+}$ ions using the Danfysik high current implanter at the University of Surrey. The $^{11}B^{+}$ ions were extracted with a potential of 30kV from the ion source and then decelerated by 25 kV at the end of the flight tube. Following the 30kV extraction lens at the end of the ion source, the ions pass through two stage magnetic analysis producing a high purity (mono-energetic and contaminant free) ion beam. In the final flight path the beam spot size and shape is defined using water-cooled silicon slits together with a combination of a magnetic and electrostatic quadrupole lenses. Only silicon is used in the slits and the defining aperture to help avoid cross-contamination from forward sputtering of metallic impurities. There is also a neutral trap incorporated in this line. The ion beam is scanned electrostatically using a triangular wave form defined by a 10MHz Wavetek function generator.

The frequencies used were 1kHz for the X scan and 1004.5Hz for the Y scan. This produces uniform implants across wafer to ±2%. However, greater non-uniformity is produced in these implants due to the focusing action of the deceleration lens.

The samples were attached to 6" wafers using photoresist and then mounted on to the deceleration lens housed at the end of the beam line in a vacuum of 10^{-4} Pa. For these implants the wafers were tilted at 7^{o}. Four doses were implanted - 2×10^{n} cm^{-2}, where n = 12, 13, 14 and 15. The instantaneous beam current density was 16 $mAcm^{-2}$, while the time-averaged beam current density was less than 0.2 $mAcm^{-2}$.

4.2.2 Anodic oxidation and etching

As discussed in section 4.1, the problem of decreasing depth resolution with increasing positron energy is attacked by remeasuring $S(E)$ after controlled etching of known thicknesses of implanted Si. This is done by anodic etching of the samples to a predetermined depth, followed by etching by hydrofluoric acid.

The simple apparatus used is sketched in figure 4.1. Any native oxide layer is first removed by dipping in HF. The sample is then dipped into the electrolyte (e.g., 90% ethylene glycol, 0.4% KNO_3 and 10% water) and the voltage supplied between it (the anode) and the cathode immediately. This electrolyte is favoured as it can be used at room temperature, and gives more reproducible results and a more accurate calibration for thin oxide growth. The current density is approximately 12.5 $mAcm^{-2}$, thus requiring a 50 mA current source for a 20 × 20 mm^2 sample. The electrolyte is constantly stirred to ensure uniform oxidation and is illuminated (often using a lamp and reflector) to enhance the anodic reaction.

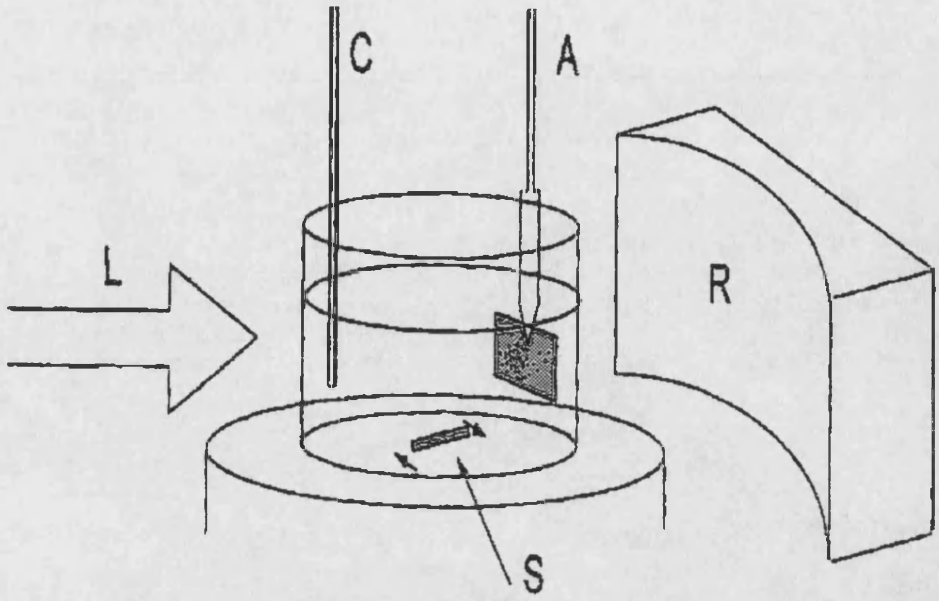

Figure 4.1: Schematic representation of anodic etching appartus. A - anode with sample: C - cathode: L - illumination: R - reflector to aid illumination: S - stirrer.

As the oxide grows the measured current decreases, and eventually stops when the applied potential can no longer pass current through the oxide layer. The equilibrium oxide layer thickness is therefore dependent on the potential V applied. The oxide thickness is measured by ellipsometry, and its variation across a 20 $\times$ 20 mm^2 sample is typically $\sim$ 10% (but can be as low as 2%). Typical results for oxide thickness are 35nm for V = 60 V and 60 nm for V = 100 V. The oxide thus grown is subsequently etched off by HF, leaving a Si surface that is H terminated. It is important to note that it has been demonstrated that the etching process does not introduce damage in the surface region to which the positrons are sensitive [45].

4.3 Results

S-parameter and etching

Figure 4.2 shows three adjacent plots of the normalised S-parameter (equation 2.10) versus incident positron energy E for the four implanted samples, before and after two etches of 40 nm and a further 100 nm (numbers A1-4, B1-4 and C2-4, respectively). Figures 4.2 (a) and (c) also have virgin Si data on them which serve to highlight visually the presence of low-momentum trapping sites, namely open-volume defects formed by the implantation of the boron ions. The data for the H-terminated virgin Si after etching (figure 4.2(c)), illustrates the change in surface S-value and the absence of detectable near-surface open-volume defects created by the etching process.

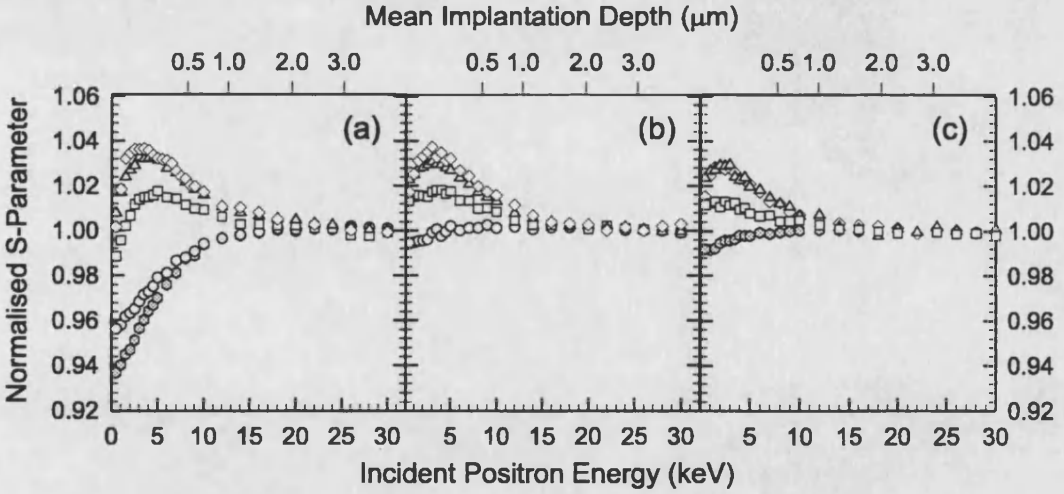

Figure 4.2: Normalised S-parameter against incident positron energy E for (a) unetched samples (A1-4 plus virgin Si), (b) samples with 40 nm etched (B1-4) and (c) samples with 140 nm etched (C2-4) and virgin Si with native oxide removed by HF etching. Shaded hexagons: virgin Si. 1).Circles: ion fluence 2×10^{12} cm^{-2}. 2).Squares: $2\times$ 10^{13} cm^{-2}. 3).Triangles: 2×10^{14} cm^{-2}. 4).Diamonds: 2×10^{15} cm^{-2}.

Looking at the plots in figure 4.2, one immediately notices a peak region centred about 4 keV. For plots A3 and A4 in figure 4.2(a), both the peak regions tend to a similar value of S_D of $\sim$ 1.04, even though the ion doses of the two differ by an order of magnitude. This is explained by the fact that a S_D value of 1.04 corresponds to saturation trapping for positrons in a medium comprised of divacancies [46, 47, 48]. Saturation trapping occurs in plots A3 and A4 in figure 4.2(a) indicating the presence of more defects in the highly doped samples whose beam fluences lie in the range 10^{14} to 10^{15} ions cm^{-3}. The data are also plotted against the mean positron implantation depth as calculated using equation 2.2. However, from the plots for the as-implanted samples A1-4 it is not possible - because of the extended positron implantation profile - to judge visually the maximum depth of the open-volume defects. After removal of material by etching of thickness equal to the projected ion range of 40 nm (as given by TRIM), it is evident that - for samples B2-4 - there are still a considerable number of trapping sites present; indeed, the near-surface defects appear still to trap almost all of the positrons, for the measured normalised S-value is close to the 1.035 seen for samples A3 and A4. Conversely, any defects left by the etching of sample A1 are at a concentration below that detectable by positrons; this can be seen visually by comparing plot B1 with the plot for the etched virgin sample shown in figure 4.2(c). Even after the removal of a further 100 nm, we still observe what appears to be close to saturation trapping for samples C3 and 4. Note also that the surface S-parameter value (i.e. at $E = 0$) increases significantly after etching, to close to unity: this is expected to be the case for an H-terminated Si surface [43].

The data for the unetched samples (A2-4) were fitted by assuming single 'box' (uniform) defect distributions (no reliable fitting could be performed for sample A1 because of the low defect concentration). The results are given in table 4.1. These fits immediately indicate that defects exist at detectable concentrations at

depths far below the ion range of 40 nm. To fit the data for the etched samples (except for B1 and C1, whose defect concentrations were below detectable limits) it was assumed that the defect concentration profile could be described by :

$$C = C_0 exp(-x/L) \tag{4.1}$$

where C_0 is the initial defect concentration at the 'new' surface ($x = 0$) and L is the decay length in nm. This assumption also includes that of a uniform defect type at all depths. For chosen C_0 and L values an exponential histogram was constructed for insertion into the program POSTRAP, using five blocks. Values used for the specific positron-defect trapping rate and defect S-parameter (S_D) were $5 \times 10^{14} s^{-1}$ and ~ 1.035, respectively [38]. Values of L and C_0 were varied until a fit was obtained giving the expected S_D for each of the five bars of the histogram. Fitting was carried out first on the sample set C2-4. It was found that two sets of L and C_0 fit the experimental curves, both giving reasonable values of S_D but with markedly differing values of L. To ascertain which of the two sets obtained was valid, a self-consistency check was performed by extrapolating back by 100 nm, the amount of the second etch, to calculate C_0 values for fits to the B1-4 data. The results of the exponential fits for both etched samples (B and C) can be found in table 4.1.

SIMS and TRIM

Figure 4.3(a) shows the implanted ion distributions as measured using SIMS and those calculated by TRIM. The measured and simulated distributions are in agreement over the first 50nm, after which the two curves diverge. The differences between the simulated and measured ion distributions is exacerbated at

Sample set	Defect concentration at surface (cm^{-3})	Depth of distribution (nm)	Decay length (nm)	Ion Flux (cm^{-2})
A2	2.5×10^{18}	340		2×10^{13}
A3	2.5×10^{19}	320		2×10^{14}
A4	2.5×10^{20}	280		2×10^{15}
B2	5.75×10^{18}		120	2×10^{13}
B3	4.75×10^{19}		120	2×10^{14}
B4	6.0×10^{19}		115	2×10^{15}
C2	2.5×10^{18}		120	2×10^{13}
C3	2.0×10^{19}		120	2×10^{14}
C4	2.5×10^{19}		115	2×10^{15}

Table 4.1: Fitting parameter for unetched samples (A) and those etched by 40 nm (B) and 140 nm (C). See text for definition of parameters.

higher fluences leading one to believe that the difference in the types of vacancy concentration profiles would also be very large.

This is shown to be the case in figure 4.3(b) which compares the TRIM vacancy distributions with the POSTRAP exponential fits to the data for the etched samples B and C in figure 1 and the single-box fits to the data for the unetched samples A2-4. The average number of vacancy-type defects per ion deduced from the single-box fits is a little over 2, compared with the TRIM result of 40. This suggests that about 95% of the vacancies initially created by the ions disappear via post-implantation migration, recombination and coalescence. The TRIM vacancy distributions in figure 4.3(b) have thus been multiplied by 0.05 for comparison with experiment. The exponential tails for samples C3 and 4 are, like the raw data, very similar; this is because the concentration of trapping sites just below 140 nm depth (the amount etched for samples C) are both near the upper limit of discrimination by the PAS technique (corresponding to saturation trapping).

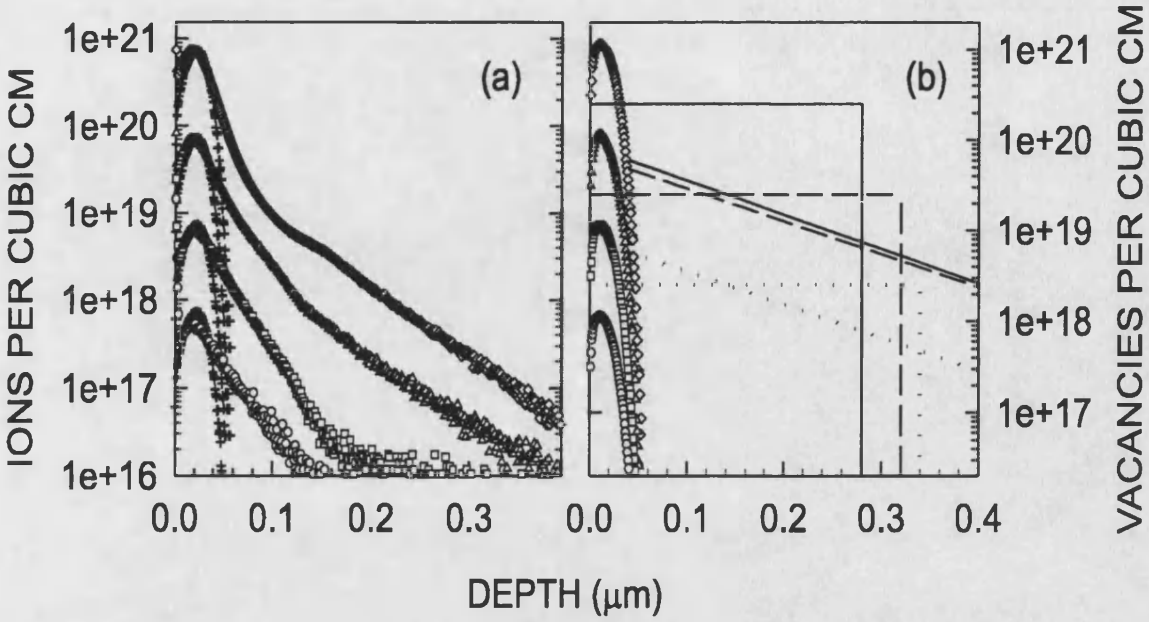

Figure 4.3: (a) +: TRIM simulations of 5 keV B+ depth distributions in Si at fluences of 2×10^n cm^{-2} where n = 12, 13, 14 and 15. Other symbols are SIMS data for the same ion fluences (same symbol convention as figure 1). (b) Symbols (convention as in figure 4.2: TRIM simulations for vacancy profiles for the four ion fluences, normalised by $\times 0.05$ (see text). Lines show box defect profiles and exponential defect tails fitted by POSTRAP (see text) for ion fluences of 2×10^{15} cm^{-2} (solid), 2×10^{14} cm^{-2} (broken) and cm^{-2} (dotted).

The ion distribution shape given by the SIMS measurement in figure 4.3(a) and the vacancy profiles given by the fitting of the positron data in figure 4.3 (b) are, on first sight, similar; the majority of ions/vacancies are in a peak in the first 50nm below the surface, followed by low-level exponential tails. However, the defect to ion concentration ratio increases with increasing depth, suggesting that the relationship between ions implanted and defects created is not simple at the deeper implant depths. This effect may be accounted for by the diffusion of defects away from the surface in the the post-implant annealing stage.

4.4 Conclusions

PAS has been used in conjunction with controlled etching to study the distribution of open-volume defects created by 5keV boron ions implanted into Si. Implant simulations from TRIM have suggested that the peak of the ion-induced defects extend to 40 nm, whereas PAS has shown that they extend far deeper than that. The loss of depth resolution associated with the broadening of the positron implantation profile has been reduced by combining the PAS technique with progressive, controlled etching of known thickness of the implanted samples. The post defect-peak ion-induced damage has been fitted successfully using an exponentially decreasing function to describe the distribution of the damage.

As well as showing its sensitivity to detecting and quantifying damage resulting from low energy, low dose implants, PAS has also shown to provide complementary information to that ascertained from SIMS measurements, showing that the defects match, and then surpass, the resting positions of the implanted ions.

Chapter 5

Equivalence of vacancy-type damage in ion-implanted Si

5.1 Introduction

We have already looked at an example detailing the extent and concentration of Frenkel defects caused by the implantation of ions into Si. However, taking positron annihilation spectra for a host of samples implanted with varying fluences of ions and then fitting the data to ascertain defect concentrations can be a fairly time consuming process. In this chapter, S-parameter profiles are measured for a wide variety of samples, implanted with various ions with varying fluences, and steps taken for formulating a relationship between S and ion dose, regardless of ion used. This could lead the way for predicting the S-parameter response, and hence defect concentration, of ions of any mass or energy implanted into Si.

5.2 Experimental Details

For this set of experiments, all the ions were implanted into n-type, phosphorous-doped (initial resistivity 40 Ωcm), Float Zone (FZ)-Si(100) at room temperature. The ions used, their energy, doses and symbols used on the plots can be found in table 5.1.

Ion	Energy (keV)	Dose (cm^{-2})	Symbol
As^+	50	$10^{10} - 10^{14}$	As10-As14
B^+	5	$2 \times 10^{12} - 2 \times 10^{15}$	B12-B15
Ge^+	120	$10^{10} - 10^{14}$	Ge10-Ge14
H^+	450	$10^{11} - 10^{17}$	H11-H17
He^+	200	$10^{12} - 10^{16}$	He12-He16
O^+	400	$10^{10} - 10^{14}$	O10-O14
Si^+	125	12	Si2-12
		1,3,5,7 $\times 10^{11}$	Si1-11 to Si7-11
		1.75,3.5 $\times 10^{13}$	Si2-13, Si3-13
		3.5 $\times 10^{14}$ (0.05 & 0.1 μA)	Si3-14a, Si3-14b

Table 5.1: Energies, doses and symbol convention used for various ions implanted into wafers of Fz-Si.

The implantations were performed 7^o off-axis and at 15^o rotation to minimise channeling effects. The current density was kept below 0.1 μAcm^{-2}, resulting in a negligible rise in substrate temperature during implantation, except for the highest-dose H^+ implantation, for which the beam current density was increased to 0.5 μAcm^{-2} and the substrate temperature was expected to increase by a few tens of degrees.

5.3 Results

Figures 5.1(a) to 5.1(g) show $S(E)$ curves for the various implanted samples used for this set of experiments. All the plots presented share broadly similar features. The data have all been normalised to the value of bulk Si (see equation 2.10). Each plot has an unimplanted (virgin) Si plot, exhibiting two annihilation sites - one at the surface ($S \sim 0.9360$) and in the bulk ($S = 1$). For the implanted samples there is a third annihilation site present corresponding to positrons trapping at vacancy-type defects induced by the implantation. This is indicated by the increase in S above unity, tending to a maximum value of 1.036, being indicative of saturation trapping. This is demonstrated for figures 5.1(a), (b), (c) and (g), corresponding to As^+, B^+, Ge^+ and Si^+ respectively. As E increases past the peaks of the said plots, S decreases as less positrons are trapped at vacancies due to the increase in their mean implantation depth.

Figures 5.1(d) and (e) show S-parameter data for damage resulting from implants of the lightest elements, namely H and He. Here, the S peaks are much broader and extend to far greater depths, especially for the H implant, as at even a high dose of 1×10^{17} cm^{-2}, saturation trapping has not been reached. This is a consequence of the much higher energy, lighter mass and greater range of this light ion as compared to the other relatively heavier ones.

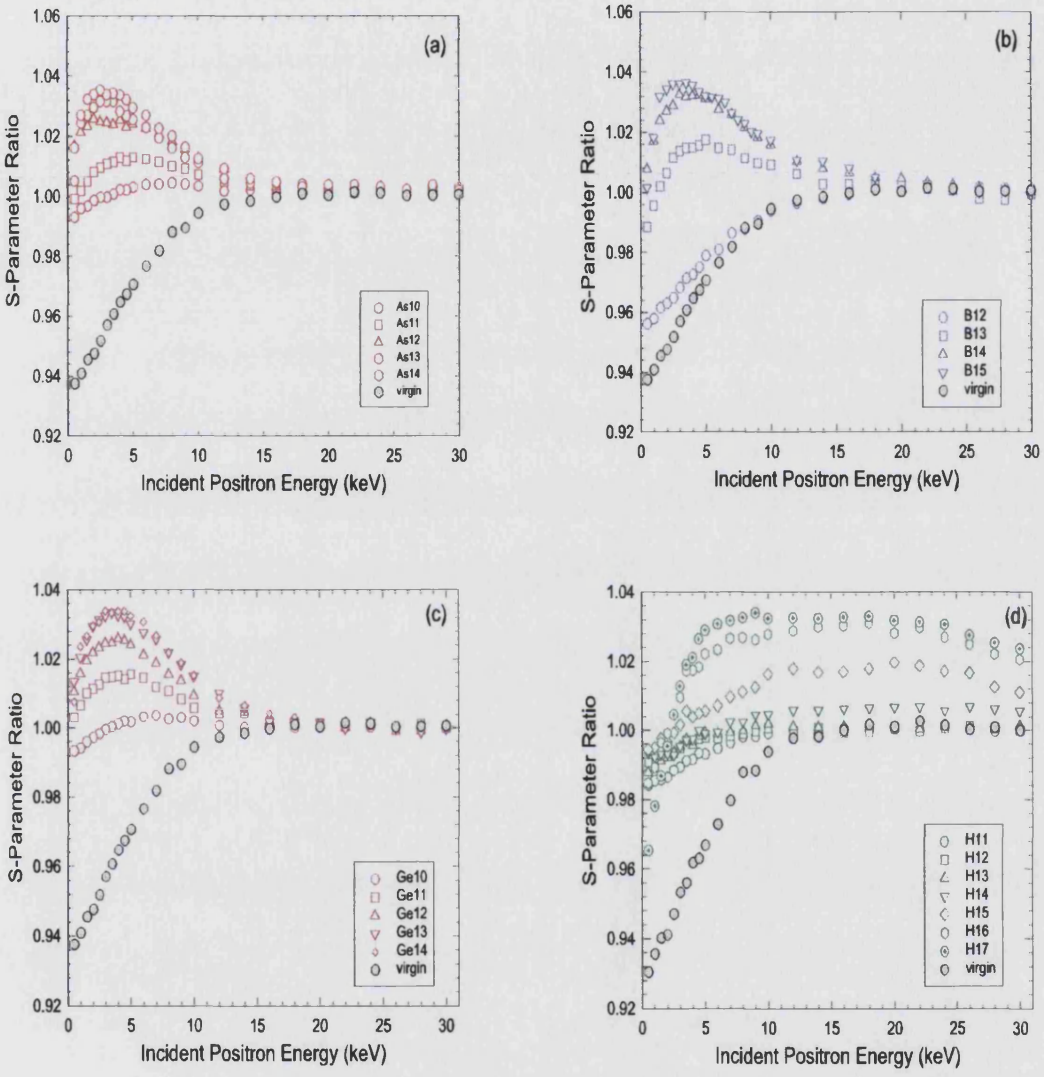

Figure 5.1: $S(E)$ for (a) 50 keV As^+; (b) 5 keV B^+; (c) 120 keV Ge^+; and (d) 450 keV H^+.

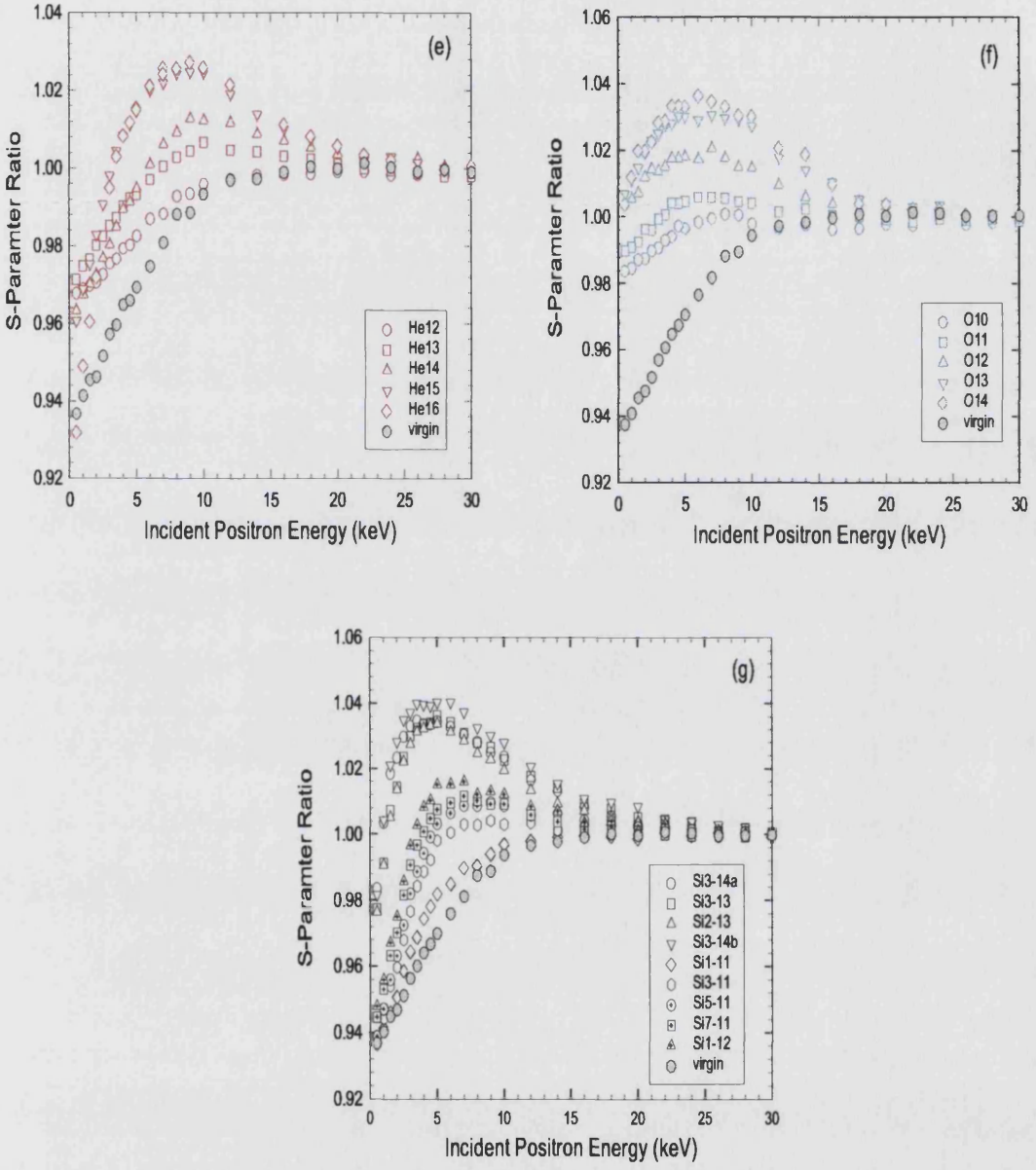

Figure 5.1: (*continued*) – $S(E)$ for (e) 200 keV He^+; (f) 400 keV O^+; and (g) 125 keV Si^+.

S-Parameter Ratios and Implant Dose

For each of the data sets, the curve corresponding to damage from the highest implant was fitted using a linear regression in order to ascertain the energy of the peak, E_p which corresponded to the region of greatest concentration of defects. The value of E_p given by the fits were 3.45, 3.45, 4.04, 8.17, 8.17, 6.4, and 4.63 keV for the As^+, B^+, Ge^+, H^+, He^+, O^+ and Si^+ sets respectively. The S value for the unimplanted Si at E_p (S_V)was taken and the following ratio determined:

$$R = \frac{S(E_p)}{S_V(E_p)} \tag{5.1}$$

When calculating values for R, it is important to recognise the influence of the surface S-parameter in determining the experimental value of $S_V(E_p)$. For the proton implanted samples, the mean implantation depth of the ions, $\overline{z}$, is 1750 nm, which also corresponds to the approximate full width at half maximum of the positron depth distribution. In the range 875-2625 nm the defect concentrations are approximately constant and there is no contribution to the measured S from surface trapping as is apparent from the value of $S_V(E_p) = S_V(18keV) = 1$.

However, for the other data sets, the same is not true. At low incident positron energies the influence of annihilation gammas resulting from positrons returning to the surface on S_S is exacerbated for the lower dose samples, as there are fewer trapping centres, meaning a greater fraction of positrons returning to the surface. There is also an observed increase in S_S for the implanted samples, which appears to be related to the change in the SiO_2 interface and is constant for much of the implanted dose range. It is necessary, therefore, to normalise the actual experimental virgin S_S to a theoretical one associated with the low dose samples.

The first step is to calculate the fraction F_S of implanted positrons which diffuse to the surface at $E = E_p$, this being deduced from:

$$F_S(E_p) = \frac{1 - S_V(E_p)}{1 - S_V(0)} \tag{5.2}$$

where $S_V(0)$ is the surface S-value for the unimplanted sample. A new value of S_S is chosen, S'_S which is consistent with $S(0)$ for the low-dose samples. $S_V(E_p)$ is recalculated as

$$S'_V(E_p) = (S'_S - 1)F_S + 1 \tag{5.3}$$

leading to the ratio being computed as $R = S(E_p)/S'_V(E_p)$.

After this correction, the low-dose limit of R is unity. The high dose limit (i.e. for saturated positron trapping) R should tend to the defect parameter S_D, the value characteristic of the principal open-volume defect in which the positrons are trapped, here assumed to be $S_D = 1.036$. While the nature of the defects is not relevant to the current set of measurements, divacancies are expected to be predominant [46, 47, 48].

It is possible for an asymptotic value $R_{max} > S_D$ to be measured if $S_V(E_p) < 1$, resulting from diffusion of the positron to the surface in the unimplanted sample but not in the high dose implant sample. Therefore it is necessary to finally normalise R so that it lies between 1 and 1.036 by using the transform

$$R' = 1 + \frac{0.036(R-1)}{R_{max} - 1} \tag{5.4}$$

R'/R decreases with ion dose in manner which compensates for the increasing effect of diffusion. The evaluated R' value as a function of dose can be seen in figure 5.2.

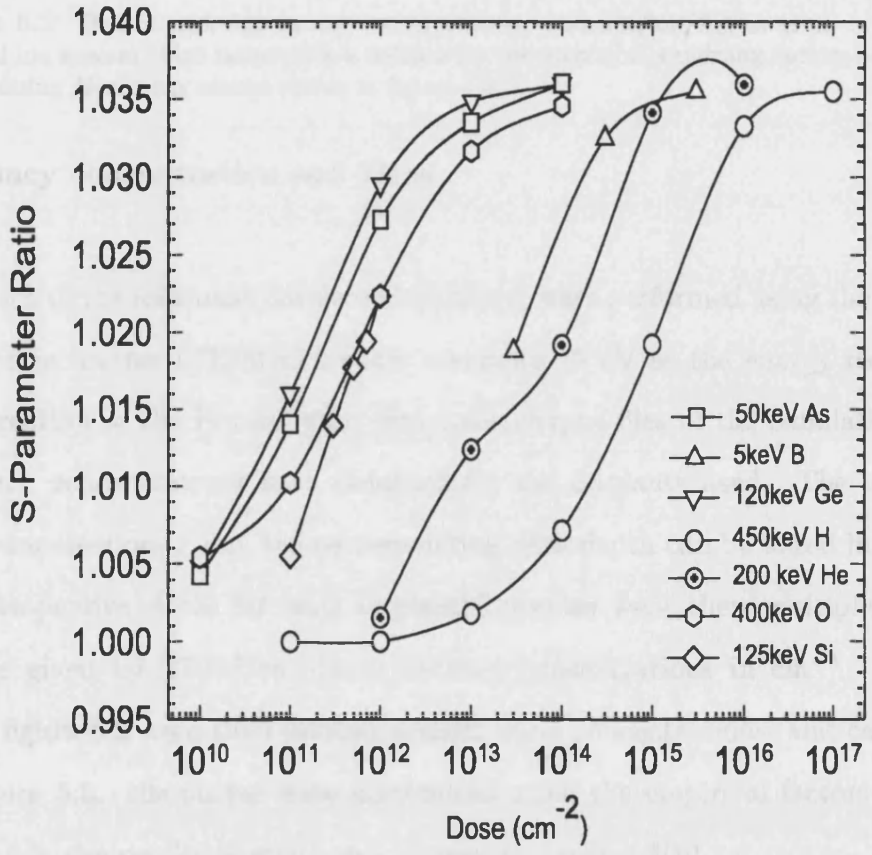

Figure 5.2: Normalised S parameter ratios (R') versus ion dose for Si implanted with As, B, Ge, H, He, O and Si ions.

Ion species	Defect Peak Depth from positron data ($\AA$)	TRIM factor Vacancies/ion/$\AA$	Empirical factor Vacancies/ion/$\AA$
As^+	1245	2.0	0.5
B^+	1245	0.272	0.0036
Ge^+	1603	1.8	0.81
H^+	16000	0.000 13	0.000 13
He^+	4946	0.035	0.0371
O^+	3347	0.192	0.192
Si^+	1994	0.65	0.189

Table 5.2: Defect peak depths and corresponding vacancies/ion/A_0, as given by TRIM, for several ion species. Also included is a column for the empirical weighting factors necessary for normalising R-vacancy curves shown in figure 5.3(a).

Vacancy concentration and Dose

For each of the ions used, implant simulations were performed using the transport of ions in matter (TRIM[41]) code, assuming 15 eV as the energy required for the creation of the Frenkel pair. From the output files of the simulations, peak vacancy concentrations were obtained for the implants used. The ions, their vacancancies/ion/$\AA$ and the corresponding peak depth can be found in table 5.2. The respective doses for each implanted species were then multiplied by the values given by TRIM to obtain vacancy concentrations in cm^{-3}. R' values from figure 5.2 were then plotted against these concentrations, and can be seen in figure 5.3. the curves were normalised using the empirical factors shown in table 5.2, the results of which can be seen in figure 5.3(b).

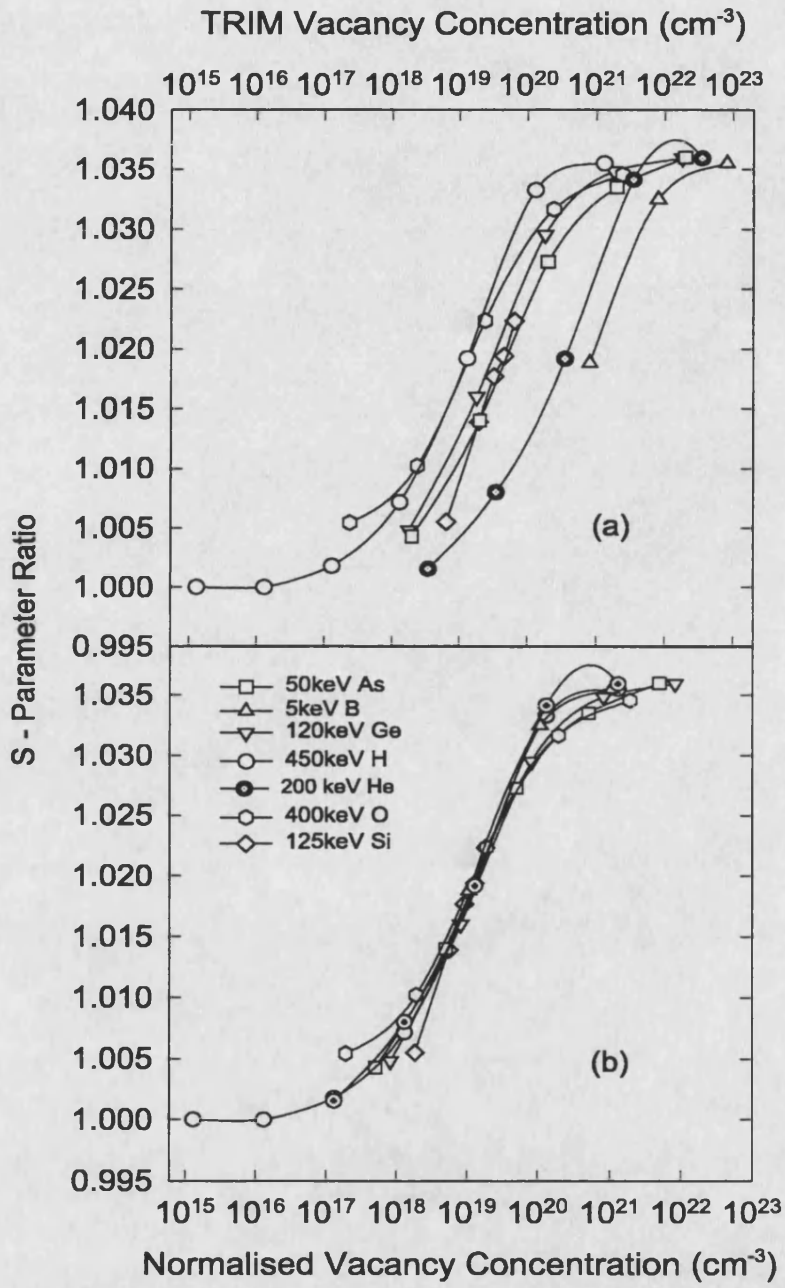

Figure 5.3: R' plotted against vacancy concentration as calculated (a) using TRIM, and (b) using factors given in Table 5.1.

5.4 Discussion

The R' values for the seven dopants plotted in figure 5.3(a) have a striking similarity following the initial normalisation procedure. The fact that the S-parameter ratios can be normalised in this way implies that the vacancy-type defects produced by the different implants are similar at low fluences in that Doppler-broadening positron measurements cannot determine significant differences, with divacancies dominating the positron trapping and no evidence of large clusters. A further significant conclusion is that the recombination of vacancies and interstitials at room temperature for the various implants are very much alike. The universality of the curves are improved by choosing empirical scaling factors, which are listed in table 5.2. This is demonstrated in figure 5.3(b). The fact that the TRIM scaling factors do not in themselves produce a perfectly universal result probably indicates the limitations of the simulations. TRIM merely calculates the number of vacancies created by implantation, but does not consider other physical processes such as recombination or coalescence.

Defect Concentrations

It is possible to calculate the concentration of a vacancy-type defects in the implanted samples to obtain an estimate of those which survive room temperature recombination. The calculation is most straightforward for the case of the H^+ implanted samples, where the fractional concentration of defects can be easily obtained assuming a two-state trapping model. The fraction of positrons trapped in defects F_D is given by:

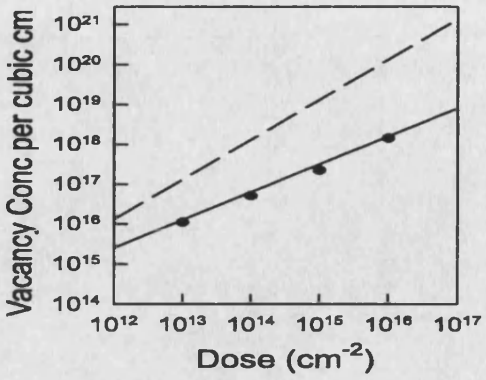

Figure 5.4: Open-volume point defect concentrations vs ion dose for 450 keV protons implanted into Si; (broken line) calculated by TRIM Data points; computed from the positron data of figure 5.1(d); (solid line) fit to positron data ($C \propto \phi^{0.7}$).

$$F_D = \frac{S(18keV) - 1}{S_D - 1} \tag{5.5}$$

where $S_D = 1.036$. The defect concentration per atom C is then

$$C = \frac{F_D \lambda}{\nu(1 - F_D)} \tag{5.6}$$

where ν is the specific trapping rate, assumed to be 1×10^{15} s^{-1} for vacancy-type point defects[49], and λ is the annihilation rate of positrons in defect-free Si (4.55×10^{19} s^{-1}). Figure 5.4 shows C vs ϕ for the proton-implanted samples calculated from the positron data and simulated using TRIM. The positron data have been fitted (solid line) as $C \propto \phi^{0.7}$, where ϕ is the implanted dose. The index 0.70 (± 0.02) indicates sublinear growth of defects with ϕ as opposed to the simple linear trend exhibited by the TRIM data - in which recombination is not modelled - indicated by the dashed line. Within this range of implant doses we observe a room temperature survival percentage of between 1% and 10%, which is in agreement with previous 2 MeV He^+-implanted Si obtained using deep level; transient spectroscopy[38].

5.4.1 Sensitivity and Precision of the technique

Threshold Fluence for detection

As well as showing that R values for samples doped with various implants show similar characteristics, PAS can be used to find the minimum ion doses to which the positron response is measurable. This can be achieved by the normalisation of figure 5.3 using the H^+ data and the ratios listed in table 5.2. These are tabulated in table 5.3 for the ions used in the present study.

Ion species	Threshold Dose (cm^{-2})
As^+	2.6×10^9
B^+	5×10^{11}
Ge^+	1.6×10^9
H^+	1×10^{13}
He^+	2.7×10^{10}
O^+	6.8×10^9
Si^+	6.9×10^9

Table 5.3: Estimates of minimum ion doses measurable by PAS using H^+ data and the scaling factors in table 5.2.

Precision

The precision of the present technique is illustrated in figure 5.5, in which R is plotted against ion dose for 125 keV Si^+ ions implanted into Si in the range 10^{11} - 10^{12} cm^{-2}. In the middle of this range a change of $2 \times 10^{10} cm^{-2}$ in ion dose leads to a change of 3×10^{-4} in R. However, there is an apparent relative deterioration in the sensitivity of the positron response to the defects created by very low energy ions - for example, the 5keV B^+ ions used in the present study (and hence only the highest-dose B^+ results are shown in the figures). This is

attributable to the effect of the surface S parameter on the $S(E_p)$ value, and hence the value of R.

When the distance between the damage peak and the surface - and hence the optimum mean positron implantation depth - is smaller than or is comparable to the effective positron diffusion length, the fraction of implanted positrons which diffuse to the surface and are annihilated from the surface state is considerable. Hence the mean S parameter is influenced significantly by S_S, and the defect value S_D has correspondingly less influence. It is felt that this effect may be attributed to defect accumulation at the Si/SiO_2 interface. The extent of the influence that this has on S_D may be reduced by etching of the native oxide using HF, and hence by normalising the value of S_S to unity, i.e. that found in the bulk of the material.

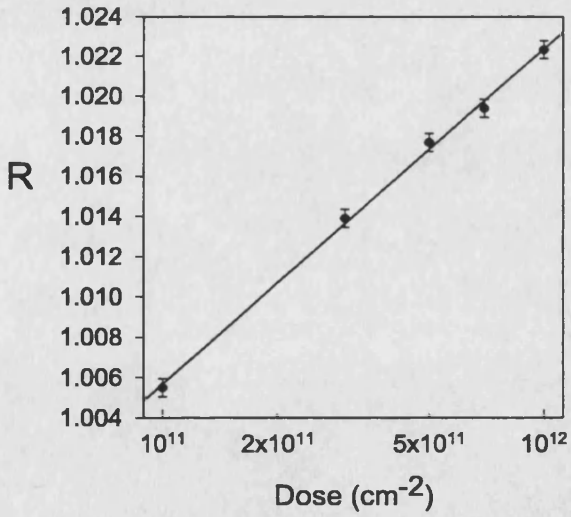

Figure 5.5: R vs ion dose for 25 kev Si^+ ions at doses between 10^{11} and 10^{12} cm^{-2}. The solid line is a fit to the data.

5.5 Conclusions

It has been shown that positron data measured from Si implanted with As^+, B^+, Ge^+, H^+, He^+, O^+ and Si^+, at varying fluences, energies and (in the case of Si^+) currents can be normalised using values of vacancy-type defects obtained from TRIM. This implies that the vacancy-type defects introduced by these implants are similar in structure and interstitial recombination rate. The potential existence of a universal $S(C)$ curve presents the prospect of predicting S parameter response and hence defect concentration (and possibly noncontact, nondestructive, *in situ* dose measurement) of ions of any mass or energy implanted into Si.

Chapter 6

Annealing of defects induced by ion implantation of Si^+ into Si

6.1 Introduction

In this section, we shall consider the effect of annealing of self-implanted Si in an *in-situ* environment. In-situ-annealing measurements of bulk defects using positron annihilation spectroscopy have been performed extensively[50, 51] but, to the author's knowledge, no work has been carried out on the annealing of near-surface defects using slow positron beams. The reasons for this are due to the problems associated with this technique. These are: (i) practical problems inherent with a high temperature filament in close proximity to liquid nitrogen cooled germanium crystal detector head, and (ii) the increasing influence on the S-parameter by S_S with rising temperature due to (a) more positrons reaching the surface as defects anneal out and (b) S_S changes as Ps is thermally desorbed.

This chapter describes a method for in-situ annealing studies which over come these problems.

6.2 Experimental Details

6.2.1 Ex-Situ Measurements

In order to gain a better understanding of annealing behaviour of defects, PAS measurements were carried out on *n*-type, phosphorous-doped (40 Ω cm), Fz-Si(100) samples, implanted with 5 $\times 10^{13}$ cm^{-2} Si^+ at room temperature and then annealed for a total of 30 s (allowing for a 1 min ramp rate) at 250, 350, 450, 550, 650, 750 and 850^{0}C. All samples were supplied by and created at the Chick Laboratory, University of Surrey.

The experimental results of $S(E)$ measurements for the samples that were annealed at the University of Surrey are presented in Figure 6.1. The peak S-parameter begins to drop between the annealing temperatures of 450 and 550^{0}C, showing this region to be the activation range for defect migration.

The data were fitted using POSTRAP[37], the results of which are shown in table 6.1. The varied fitting parameters were the defect concentrations and their depths, modelled by a single box, until there was (a) a good visual fit and (b) the calculated defect S-parameter was 1.036, a typical value for saturation positron trapping in Si divacancies. There are no defect concentration values given for the 750 and 850^0 samples. Looking at figure 6.1, the initial parts of the curves of both aforementioned samples have higher S values than the 650. As it is unlikely

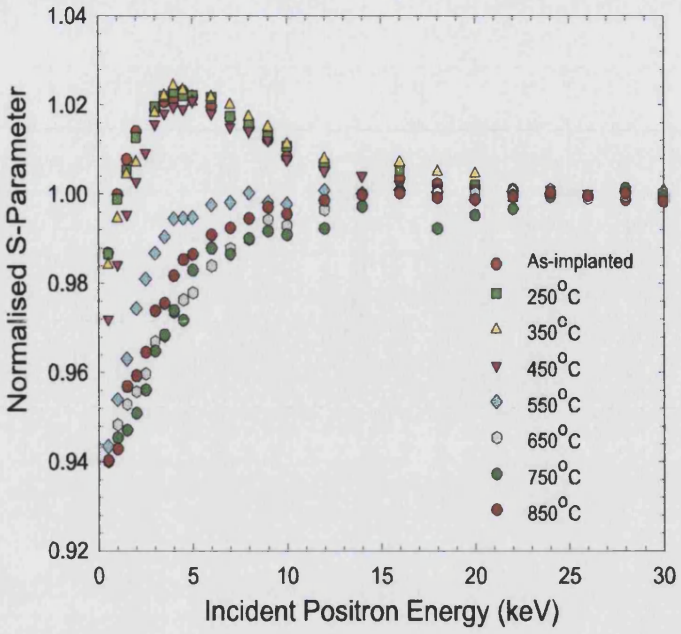

Figure 6.1: Normalised $S(E)$ for Si implanted with 50 keV Si^+ at a flux of 5×10^{13} cm^{-2}, and then annealed at the temperatures denoted by the legend.

that annealing to higher temperatures creates more defects, it seems as if this has induced a change in the surface or near-surface state that has caused the overall S-parameter to increase. This makes the results of any subsequent fit meaningless, as doing so leads to a higher defect concentration than for a sample annealed at a lower temperature.

This type of experiment is typical of all the previous work carried out using the slow positron beam. In order to develop a greater understanding of the defect migration, an as-implanted piece of Si was annealed, in-situ.

Annealing Temperature(^oC	Box Depth(A^o $\pm 500A^o$	Defect Concentration (cm^{-3})
As-implanted	2500	4.8×10^{19}
250	2500	5.2×10^{19}
350	2500	4.5×10^{19}
450	2500	4.8×10^{19}
550	2500	5.5×10^{18}
650	2500	1.3×10^{17}
750*	2500	2.7×10^{17}

Table 6.1: Defect concentration from fitting of data using a single box fit. *C_D for the 750 anneal is higher than the 650 due to an increase in S_S state affecting S_{peak}.

6.2.2 In-situ Measurements

Experimental Details

The modified sample heater assembly used for these measurements was described in Chapter 3, section 3.3.2.

To study how the defects evolved with temperature, it was not necessary to take S-parameter measurements at all incident positron energies, but simply a few key ones - namely 0.15 keV (at which one assumes that all positrons are annihilated at the surface), $\sim$ 5 keV (chosen to match the peak response to the subsurface damage), and 30keV (all annihilations assumed to be in the undefected bulk material). The maximum value of S (S_{peak}) corresponding to the maximum response to the damage, is the most important value in attempting to quantify defect migration; the bulk value (S_{bulk}) is necessary for normalisation of data, especially as there may be infrequent shifts in the data taken; and knowledge of the surface S value, $S_{surface}$, is important because it influences the value of S_{peak}.

Measurements at increasing temperature were collected with the chosen beam energies of interest. However, when the sample temperature had been increased to around 350°C and the beam energy was 30 keV the annihilation gamma signal counts dropped considerably. It was discovered that during the heating process electrons were leaving the filament on the heating-rig and were accelerated towards the source; this resulted in (a) charging of elements near the source leading to an electric field which deflected the positron beam off its path, and/or (b) a current passing through the moderator/source assembly to the batteries supplying their potentials, thereby decreasing the potentials to levels not appropriate for the beam optics. To overcome this problem, two steps were taken. Firstly, a stainless steel foil was placed around the sample and heater, at ground potential, to prevent a great proportion of the electrons emitted by the filament from escaping into the beam line; it also acted as a heat shield for protecting the detector. Secondly, a 92%-transmission tungsten mesh was placed in the beam line, approximately 25cm from the sample, with a potential of -800V applied to it, preventing electrons from reaching the source end of the beam and flooding the moderator (the filament was held at -600V during heating).

6.3 Results

Below are outlined details of the various experimental results attained and charts evolving in the understanding and interpretation of them.

6.3.1 S-parameter Results

It was decided that it was only necessary to collect spectra at three data points, namely $S_{surface}$ at 0.15 keV; S_{peak} at 4.2 keV; and S_{bulk} at 30 keV. Figure 6.2(a) shows the results of the S-parameter vs annealing temperature measurement at the three aforementioned energies.

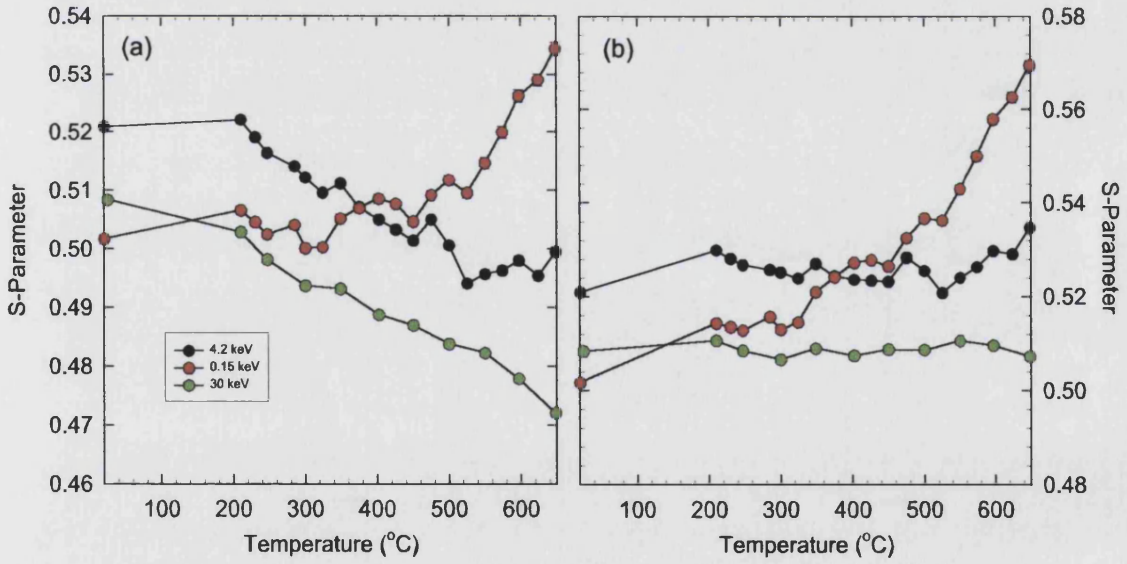

Figure 6.2: (a) As measured S-parameter against temperature for self-implanted Si annealed in-situ. (b) Normalised S-parameter against annealing temperature for self-implanted Si with a correction for the decreasing S_{bulk} shown in (a).

The first thing one notices is the decline of S_{bulk} with increasing temperature. Although the detector head was withdrawn by a few cms from its usual position, the proximity of the heater to the detector (5cm) with only a thin stainless steel re-entrant tube separating the two meant that the resolution of the detector suffered. Making a correction to the bulk S-parameter so that all $S_{bulk} \approx 0.509$ and then applying the same correcting factors to S_{peak} and $S_{surface}$, the data have the form depicted in figure 6.2(b). There is no decrease in either the bulk or peak S-values, but there is a large rise in the surface S-value. At elevated temperatures, implanted positrons that diffuse back to the surface can be desorbed from the surface state by binding to an electron and escaping as positronium. The subsequent para-positronium (p-Ps) annihilation gammas will contribute to the photopeak, increasing the S-parameter. To evaluate, and correct for, the contribution of p-Ps formation, and hence the increasing $S_{surface}$, one needs to calculate the increase in the fraction of positrons returning to the surface, F_S.

Calculating F_S from signal count rates

To evaluate F_S one can measure the variation with annealing temperature of the total counts in the Ge detector photopeak for an incident positron energy ($E = 4.2$ keV) at which the mean depth probed corresponds to the region where the defects are most densely distributed. Also measured are the total photopeak counts for incident positron energies at which 100% or 0% of the incident positrons are assumed to encounter the sample surface, ($E = 0.15$ keV and 30 keV, respectively) (Figure 6.3). Assuming that the decrease in counts detected at higher temperatures is due to an increase in the number of positrons returning to the surface and forming o-Ps, and not to an increase in the number of epithermal positrons leaving the surface (the temperatures involved are not sufficient to raise the energy of the epithermal positrons significantly), then F_S

is given by:

$$F_s = \frac{C_B - C_P}{C_B - C_S} \tag{6.1}$$

where C_B, C_P and C_S are photopeak counts for the $E = 30$, 4.2 and 0.15 keV, respectively (subscripts stand for bulk, peak and surface). Figure 6.4 contrast fraction of positrons returning to the surface as calculated by the empirical method outlined above and that given by the output of the program POSTRAP applied to the fitting of the ex-situ data discussed in section 6.2.1.

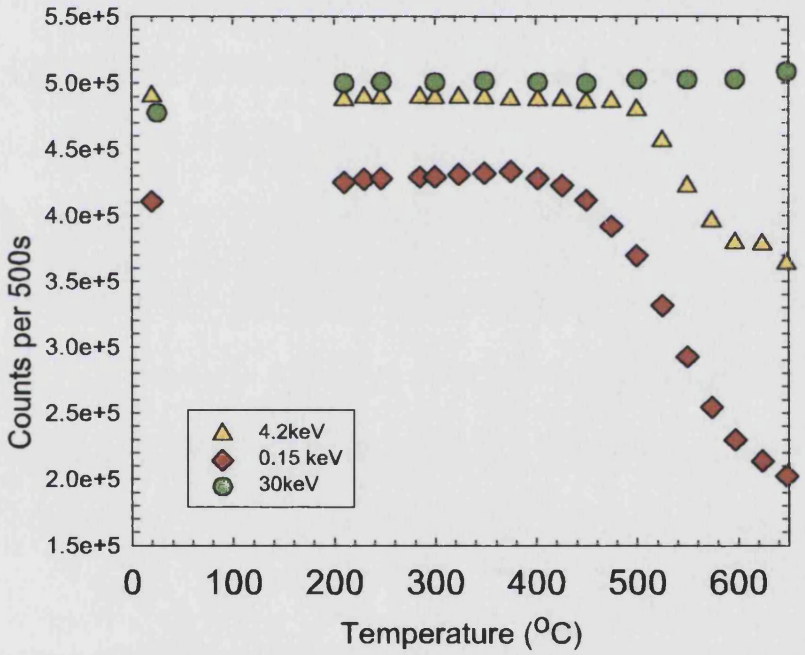

Figure 6.3: Photopeak counts measured over 500s against annealing temperature for three incident positron energies.

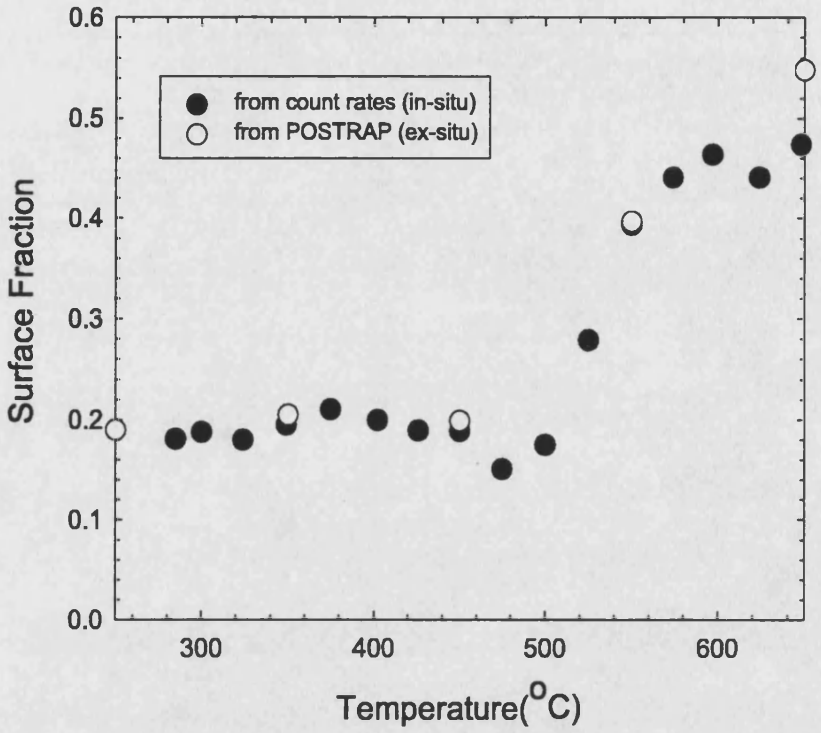

Figure 6.4: (Fraction of positrons implanted at 4.2 keV returning to the surface. Full circles: computed from count rates measurements taken in-situ (figure 6.3). Open circles: computed from POSTRAP analysis of ex-situ data.

S_{peak} values were then corrected using F_S (figure 6.4) by subtracting from the measured values the correction factor $(F_S - F_{SL})(S_S - S_{SL})$, where F_{SL} and S_{SL} are the low-temperature asymptotic values of F_S and S_S, respectively.

The corrected S_{peak} is plotted against annealing temperature in figure 6.5. The results show the annealing of the vast majority of defects within a few tens of degrees around 500°C.

These data were, however, only obtained after much massaging of the data and the use of F_S to correct $S(T)$. It is clear that F_S itself contains equivalent information on defect annealing behaviour and later work (described below) concentrates

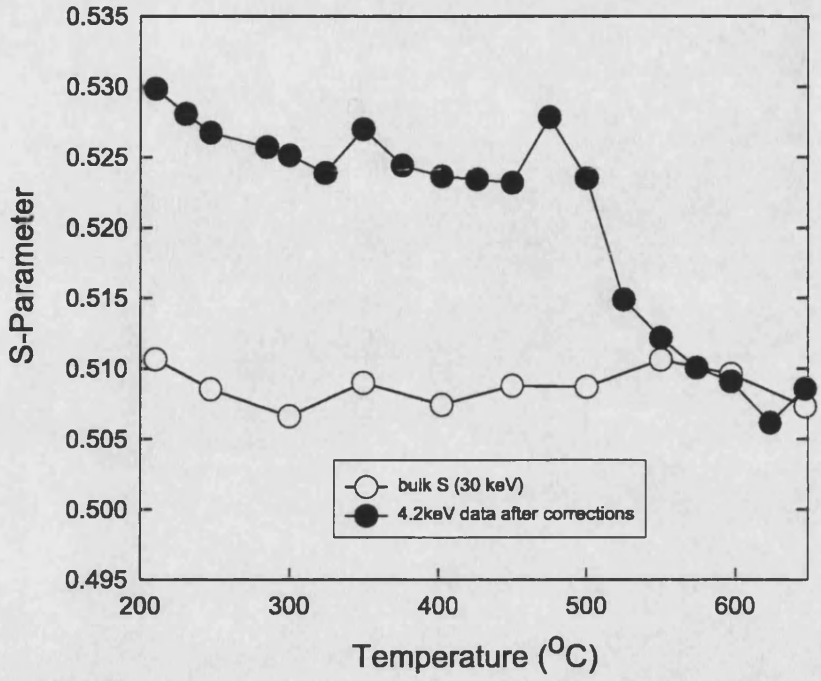

Figure 6.5: S-parameter against temperature for self-implanted Si after all corrections have been made.

on its evaluation. The method described above for measuring F_S is not ideal because it assumes that (a) the incident positron beam intensity is identical at the three energies used, and (b) that back-scattering and epithermal positron emission has no effect on the count rates. Both conditions are not generally satisfied, and both are difficult to correct for experimentally. It was therefore felt that a better way of estimating F_S would be to measure the fraction of positronium formed, remembering that this is only possible at the surface (see section 1.2.3).

6.3.2 Positronium fraction - 1st attempt

A few months after taking the initial set of in-situ annealing data on the Si^+ implanted Si described above, it was decided to look again at the annealing of near-surface defects in Si^+-implanted Si by evaluating $F_S(T)$ via measurement of positronium (Ps) formation fractions - i.e., of the ratio of photopeak-to-valley ratios in the Ge detector gamma ray energy spectra (see section 2.2.9). This technique has several benefits over measuring the peak S-parameter in-situ, namely:

- a loss in detector resolution with increased temperature was not an issue as it was only counts in the photopeak and valley being measured, not the extent of peak broadening:
- the comparatively short data acquisition times required (100s) in order to obtain sufficient counts for good statistics;
- the need for only one measurement at 30 keV at low temperature, this value being ample for subsequent F_S calculations (see equation 6.2).

An $S(E)$ measurement was carried out prior to the in-situ anneal to ascertain the value of S_{peak}; the figure was chosen to be 3.3 keV, somewhat lower than the value found previously.

The production, and detection of, Ps has been outlined in sections 1.2.3 and 2.2.9. It is assumed that Ps can only be formed at the Si surface. Figure 6.6(a) shows the variation of counts in the Ge detector photopeak with temperature at 0.15 keV (surface) and 3.3keV (peak); this is equivalent to the results shown in figure 6.3 earlier. Assuming no increase in the number of epithermal positrons

as the sample temperature is increased [52], and that the drop in counts for the 0.15 keV positrons is due entirely to o-Ps formation, then the fractional increase in positrons returning to the surface, F_S is given by equation 6.1 F_S obtained in this way is plotted in figure 6.6(b).

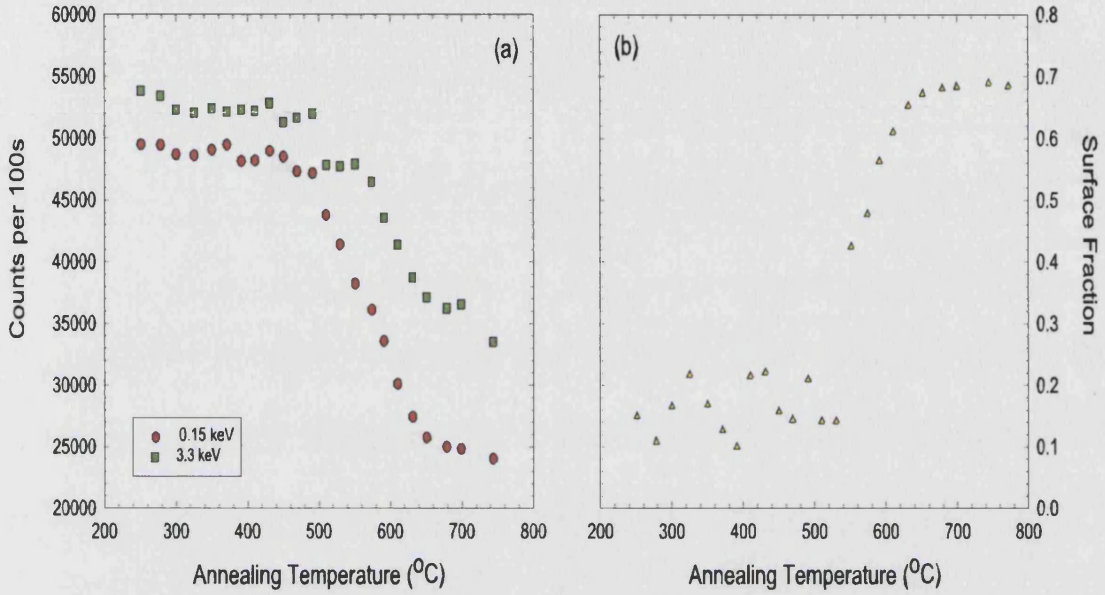

Figure 6.6: (a) Photopeak counts over 100s against annealing temperature for self-implanted Si as calculated from P:V ratios. (b) Fractional increase in positrons returning to the surface as calculated using equation 6.1.

F_S can also be determined by measuring F_{Ps}, the fraction of positrons returning to the surface which form Ps. R_F, measured as a function of annealing temperature, is defined as the ratio of counts in the valley (i.e. between approximately 400 and 500 keV), to counts P_F in the photopeak itself. By determining these figures when no Ps is formed (F_{Ps}=0; low temperature, 30keV) and when all the positrons annihilate as Ps (F_{Ps}=1; high temperature, 0.15keV), absolute intermediate values for F can be determined [18] from the equation:

$$F_{Ps} = \left[1 + \frac{R_1 - R_F}{R_F - R_0} \cdot \frac{P_1}{P_0}\right]^{-1} \tag{6.2}$$

where $R_F = (T_F - P_F)/P_F$ and T_F represents the total counts in the range 400 to about 520 keV. R_1, P_1, R_0 and P_0 are the ratios and peak counts for $F_{Ps} = 1$ and 0, respectively. Figure 6.7(a) shows the fraction of positrons, implanted with 3.3 and 0.15 keV, returning to the surface and forming o-Ps. The surface fraction is calculated by taking the ratio of the fraction forming o-Ps at 3.3 keV to that at 0.15keV, and is plotted in figure 6.7(b). As stated earlier, the second method is superior to the peak count method because it is not affected by changes in count rates. It does, however, assume that epithermal positrons (0.15 keV) do not significantly affect the R_F measurement.

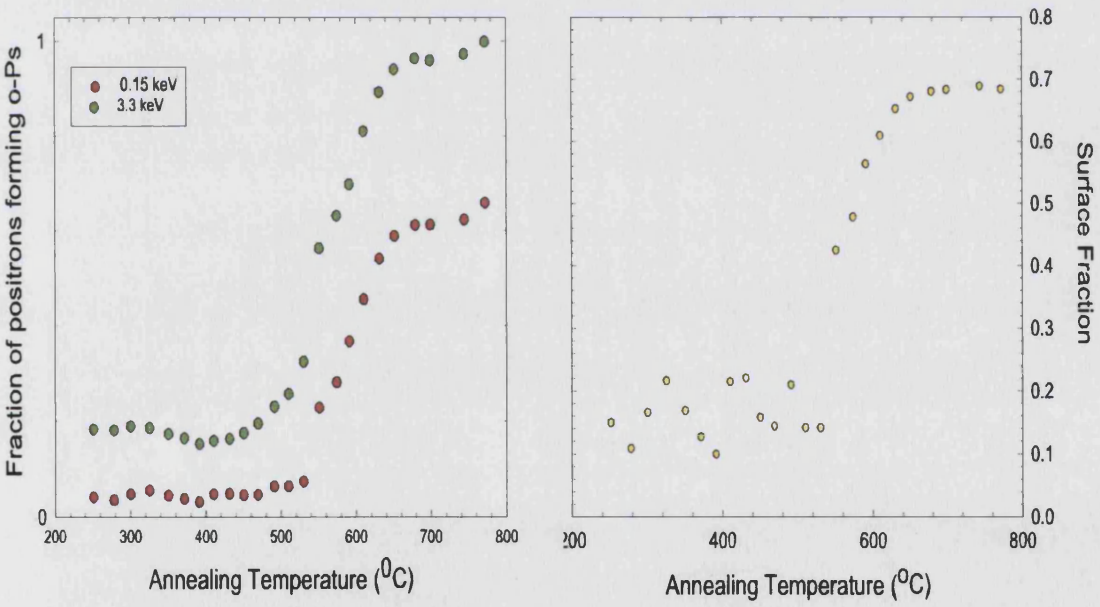

Figure 6.7: (a) Increase in the fraction of positrons implanted at 3.3 keV and 0.15 keV returning to the surface and forming o-Ps as calculated from the ratios R. (b) Increase in fraction of positrons returning to the surface implanted at 3.3 keV as calculated from ratios at various temperatures.

6.3.3 Positronium Fraction - 2nd attempt

After having calculated F_S with the aforementioned method, it was realised that there were a few improvements that could be made. Assuming that the measured positronium fraction at 0.15 keV, at high temperatures, would be equivalent to that for 100% Ps formation was incorrect. Howell *et al* [53] stated that at low incident positron energies, the positronium produced by epithermal positrons being ejected from the surface may be more intense than that formed by the diffusion of thermalised positrons to the surface. This would require a re-evaluation of P_1 and R_1 in equation 6.2.

Knights *et al* [54] showed that as the incident positron energies decreases below 1 keV, the epithermal fraction increases steeply from almost zero to nearly 100% as E approaches 0 keV. In order to calculate P_1 and R_1, Ps fractions were thus measured at 1,2, 3 and 4 keV on a piece of unimplanted Si at high temperatures, and the required values extrapolated from $F_{Ps}(T)$ plots, as shown in figures 6.8(a) and (b).

The value used for R_0 was calculated using a 30 keV measurement on the implanted sample, a year previous to the attainment of P_1 and R_1. It was necessary, therefore, to compare R_0 values obtained from the two silicon samples and applying a scaling factor of 96% to the more recently derived values of P_1 and R_1.

Branching Ratios

In order to elucidate the fraction of positrons returning to the surface from the measured positronium fractions, one needs to calculate the branching ratios, η,

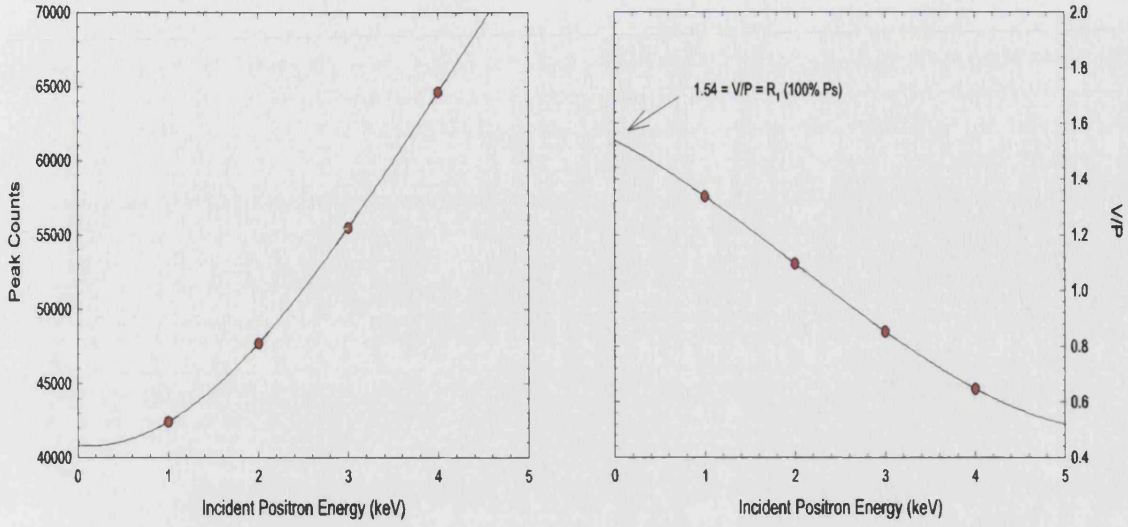

Figure 6.8: (a) Peak region counts measured on virgin silicon at 747°C, taken at select energies, extrapolated to ascertain 100% Ps formation peak value, P_1. (b) V/P values for positrons incident at various energies, measured at 747°C, with points being extrapolated to calculate V/P for 100% Ps formation, R_1.

at the surface. Assuming that the native oxide surfaces of both the virgin and implanted silicon samples are the same, then a value of η calculated for one system will be valid for the other. If the fraction of positrons returning to the surface forming positronium is given by:

$$F_{Ps} = \eta \cdot F_S \tag{6.3}$$

then one has a value for η. Once derived from measured F_{Ps} and calculated F_S values (the technique for doing so is outlined below) for virgin silicon, F_S for the implanted sample at varying temperatures was determined, leaving one final step to cipher a defect density profile.

6.3.4 Calculating defect densities from F_S

For all the acquired data to be of any quantitative worth, one needs to evaluate defect densities from surface fraction calculations. From equation 2.4 and 2.5 we can express the effective positron diffusion length, L_{+eff} as:

$$L_{+eff} = L_{+}\sqrt{\frac{\lambda_b}{\lambda_b + \nu C_d}} \tag{6.4}$$

where L_+ is given by fitting of a virgin sample using VEPFIT and C_d is the defect concentration per atom.. The fraction of positrons, implanted with energy E, to a mean depth $\overline{z}$, returning to the surface is given by:

$$F_S = \int_0^\infty P(E,z)e^{-z/L_{+eff}}dz \tag{6.5}$$

where $P(E,z)$ (see equation 2.1) is defined as the fraction of positrons entering the solid with initial energy E that will be stopped at depth between z and $z+dz$. By entering a range of C_d values in a Sigmaplot [55] worksheet, a corresponding range of surface fraction values are calculated.

Both the positron diffusion length, L_+, and the trapping rate, ν, are temperature dependent. In present calculations these were taken to $T^{-1/4}$ [9] and $T^{-1/2}$ [56], respectively. The latter dependence has been seen to vary greatly, and to depend on defect size; however, these variations have only a second-order effect on the present analysis.

L_{+eff} was calculated at each annealing temperature, giving a range of $F_S(T)$ values vs C_d from which the relevant points were chosen.

Defect Concentration Profiles

All in all, 5 different methods were employed to obtain F_S plots against annealing temperature, as can be seen in figure 6.9. To re-iterate, the various techniques used were:

i Output of POSTRAP from the fitting of the ex-situ data

ii Comparing photopeak count rate measurements at peak and surface energies, taken from the in-situ S-parameter data

iii Comparing photopeak count rate measurements at peak and surface energies, taken Peak and Valley count rate measurements

iv As derived from Ps fraction measurements, assuming no significant epithermal contribution to Ps emission

v As derived from Ps fraction measurements, using unimplanted Si to calculate high temperature branching ratios

All plots exhibit broadly similar properties, all having the same form, and showing the points of inflection at equivalent temperatures. This suggests that all the techniques employed are conveying qualitatively equivalent information about the temperature-dependent behaviour of the defects. However, Howell *et al*[53] have suggested that there may be more Ps produced from epithermal emission than that produced by the diffusion of thermalised positrons to the surface at high

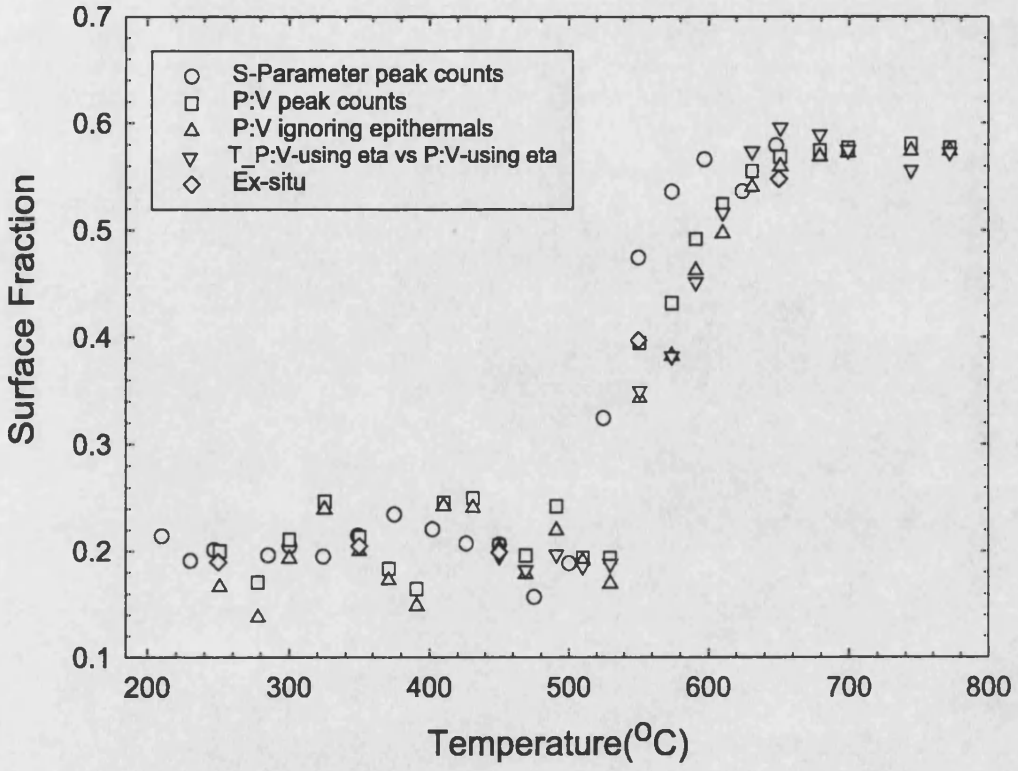

Figure 6.9: Plot showing F_S against annealing temperature, as derived from the 5 different methods described in the text. The data have been normalised to the high and low temperature limits of the ex-situ fit for the purpose of comparing the shapes of the curves.

temperatures. This implies that data obtained using a 0.15 keV measurement for 100% Ps formation is contaminated by epithermal Ps formation and, therefore, means that method (v) outlined above is the most valid.

Figures 6.10(a) and (b) compare and contrast $F_S(T)$ and $C_d(T)$ plots for the data obtained from the fitting of the ex-situ data using POSTRAP and that obtained from Ps fraction calculations. Both F_S curves exhibit similar shapes, although they disagree on the low temperature returning surface fraction. The effect of this difference can be seen in figure 6.10(b) where the low temperature defect concentrations disagree considerably. The $C_d(T)$ curves tend towards agreement

at high temperatures where the majority of defects have annealed out and the disparity between F_S is not as prevalent.

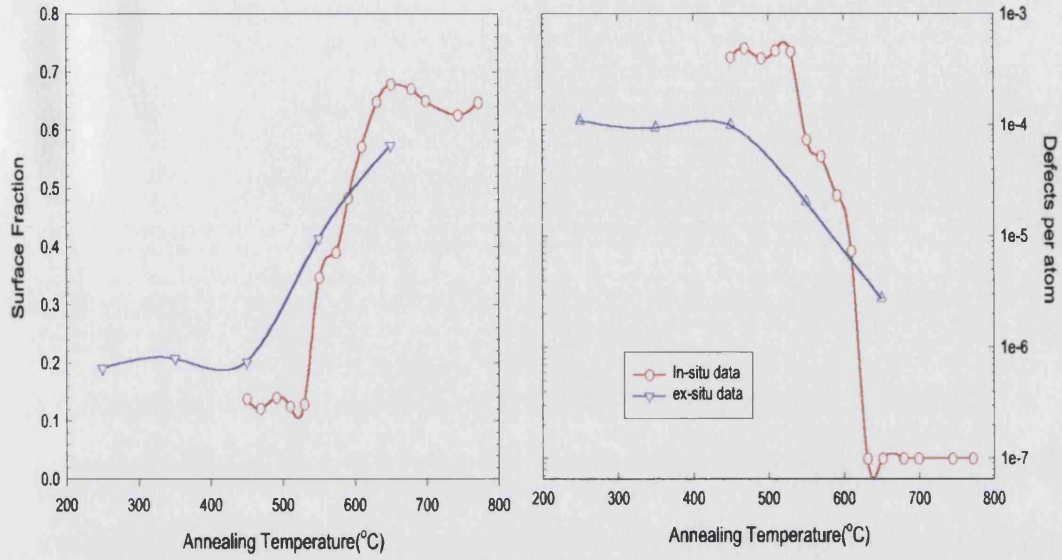

Figure 6.10: (a) Fraction of implanted positrons returning to the surface as calculated from the output of POSTRAP and from Ps fraction measurements. (b) Defect concentration profiles as given by POSTRAP and from Ps fraction measurements.

6.4 Discussion

The fraction of positrons returning to the surface as calculated at low temperatures is affected greatly by the value of the constants used in equation 6.2. The constants that were calculated from measuring Ps fractions on virgin silicon were scaled by 96% to account for systematic changes that had taken place between the original measurement on the implanted silicon and the subsequent one on the virgin silicon.

If, for argument's sake, we take a scaling factor of 90%, we get a low temperature

F_S value of about 20%, which is comparable to the ex-situ fitting output, and, consequently, attain a C_d value of 1×10^{-4} defects per atom, again comparable to the ex-situ fitting results. Therefore, the first explanation between the disparity ex and in-situ results is direct consequence of the 100% Ps formation regime values employed.

Another possible explanation is a different physical environment for the positron in the ex and in-situ states with the latter's elevated temperature decreasing the positron diffusion length (by a factor $T^{-0.25}$), resulting in fewer positrons returning to the surface. This would then be interpreted as the presence of a larger number of defects. There was a concern that because the surface of the samples used were not atomically clean, i.e. they had their native oxide layers on them, that this would affect F_{Ps}. In fact, our results agree quite closely with Ps fraction measurements carried out by Mills [9] on clean Si samples.

6.5 Conclusions

The in-situ annealing of self-implanted silicon has been used to investigate the temperature dependent behaviour of defects. The shape of the defect profile obtained from Ps fraction measurements in an in-situ annealing environment have been shown to be similar to that obtained from the fitting of ex-situ annealing data. The technique has shown that it is possible to pin down the range of temperatures over which the defects anneal out, both quickly and accurately.

Although the development of a reliable method for observing in-situ annealing of near-surface defects was the main aim of the research described in this chapter, it

is interesting to note that for the particular implanted sample used in these studies the defects annealed, apparently in a single annealing stage, at approximately 550°C. This temperature is considerably higher than that accepted for divacancy annealing, and suggests that the defects in our sample were not simple divacancies but were prevented from migrating until 550°C by the formation of some form of complex. Further work on in-situ annealing would be informative.

Chapter 7

Defect Studies of Laser Irradiated and Hydrogenated 4H-Silicon Carbide

7.1 Introduction

Research on SiC is driven by the growing promise of applications in blue light diodes, integrated circuits operating at high temperatures, high power/high frequency devices and quantum structures. The ability of SiC to function under extreme conditions is very much dependent upon the structure of the crystal lattice. Quantitative analysis of PAS has proved to be an invaluable tool in the detection and identification of open-volume defect distributions with the material [57, 58, 59, 60].

The majority of experimental studies of vacancy-type defects in semiconductor structures have been carried out on as-grown and ion-implanted samples. Little or no work has, to the author's knowledge, been reported on laser-irradiated materials. In the present study near-surface structural changes induced by excimer lasers at two wavelengths and a range of fluences have been investigated by PAS in conjunction with photoluminescence (PL) spectroscopy.

Laser annealing is an extremely rapid heating technique: at the highest temperature reached ($> 1700\ ^oC$) the SiC lattice can be amorphised. In addition, if the laser wavelength is low enough amorphisation can occur at much lower radiation fluences because the photon energies are sufficient to break bonds in the near-surface region of the material.

7.2 Experimental Details

7.2.1 Sample Preparation

4H-SiC samples from Cree Research Inc. were cut into three squares $\sim 6 \times 6$ mm from a 35 mm diameter wafer. The first wafer consisted of a 3μm thick epitaxial layer, whereas the other two were bulk samples; all were silicon face. An ArF excimer laser, with λ=193nm and pulse duration $\sim$25ns was used to modify the surface and sub-surface regions of the first wafer. The other two wafers were irradiated with a XeCl excimer laser, with λ=308nm and of similar pulse length as the ArF laser. Each quarter of each of the four wafers was irradiated at different fluences (except one in which a corner was left unirradiated so that it would act as a reference sample); the complete details of the samples can be

Sample	1	2a	2b
Growth	Epi/Bulk	Bulk	Bulk
Thickness (μm)	3/330	345	345
Doping (cm^{-3}	$2\times10^{16}/5\times10^{18}$	2.6×10^{16}	2.6×10^{16}
Orientation	8^o Off	8^o Off	8^o Off
Polarity	p-type	n-type	n-type
Fluence (Jcm^{-2})	1.1, 1.2, 1.3, 1.4	1.4, 1.5, 1.6, 1.8	1.1, 1.2, 1.3, Ref
Wavelength (nm)	193	308	308

Table 7.1: Laser irradiated 4H-SiC wafer fabrication parameters for the four samples investigated.

found in table 7.1. All the wafers were mounted in chambers which were flushed with argon prior to irradiation. The pressure during irradiation was 10^{-6} and 10^{-4} Torr for the first and the next two wafers respectively. The samples were irradiated with laser fluences in the range 1.1-1.8 J cm^{-2} with 10-50 laser pulses.

Following irradiation the samples were hydrogenated in a capacitively coupled r.f (13.56 Mhz) excited plasma. The chamber was evacuated to a pressure of 10^{-6} Torr and back filled with hydrogen. The level of hydrogenation was achieved via control over power density and exposure time.

7.2.2 Photoluminescence (PL) spectra

The PL spectra were recorded using the multi-UV lines (333.6 to 363.8 nm) of an Ar^+ laser. At these wavelengths the penetration depth of the laser radiation is estimated to be between 3 and 5 microns. Therefore, in the case of sample 1, some of the radiation will probe across the substrate/epitaxial interface. The beam was moderately focussed with a power density of $\sim$20 Wcm^{-2} and dispersed

using a SPEX 1404 double grating monochromator fitted with two holographic gratings blazed at 500 nm with 1200 grooves mm^{-1}. The PL-signal was detected using a photomultiplier tube in conjunction with a conventional lock-in amplifier arrangement.

7.2.3 Alterations to the positron beam

Owing to the relatively small irradiated sites on the samples (approximately 2×2 mm), it was necessary to install an aperture, of diameter 2mm, directly in front of the source. This had the effect of not only reducing the beam size by a quarter, but also of decreasing the intensity of the beam to $\sim \frac{1}{5}$ of what it was originally. This meant that the data acquisition times had to be increased significantly from 500s a point to 2000s. Care had also to be taken when positioning the beam on the sample as a misalignment of only a few tenths of a millimetre would mean that the beam would 'leak' onto a section of the sample that had been irradiated with a different fluence to that which was being studied. This experiment probably demonstrated the absolute physical limit of sample size that one could take meaningful measurements on using the present experimental setup.

7.3 Results

PAS and PL spectra were taken for the two irradiated sample sets; sample 1 which was irradiated with 193nm pulses at fluences between 1.1 to 1.4 Jcm^{-2} and samples 2a and 2b which were irradiated with 308nm pulses at fluences between 1.1 and 1.8 Jcm^{-2}.

7.3.1 Laser Annealing by 193nm Pulses

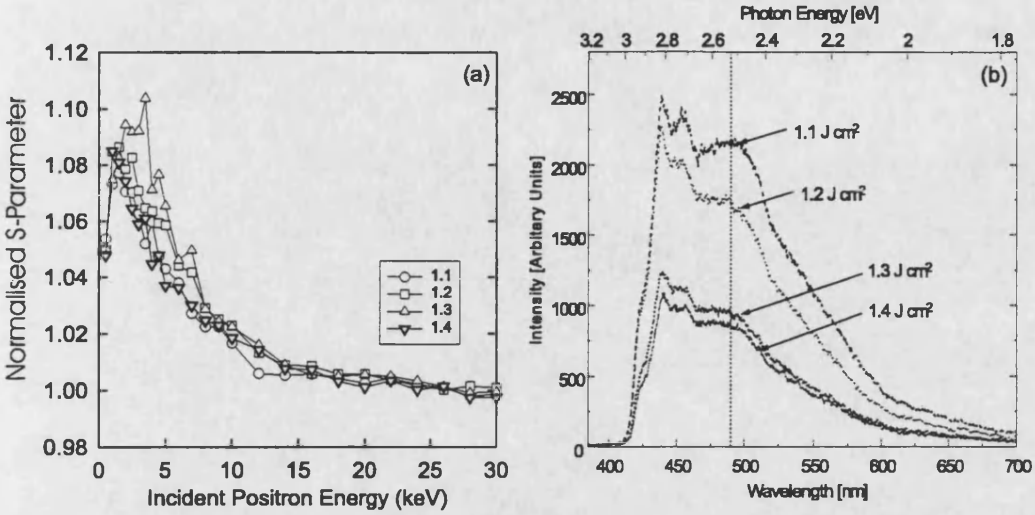

Figure 7.1: (a) Normalised S-Parameter profile of a sample of 4H-SiC irradiated with laser pulse of λ=193nm, at four sites on the same sample which correspond to four different irradiation fluences. (b) Photoluminescence spectra for the same sample as described in (a) with the addition of a reference sample Data for unirradiated sample are shown in Fig. 7.2.

Figure 7.1(a), shows the positron spectra for 4H-SiC irradiated with 50 pulses at a pressure of 10^{-6} Torr at λ=193nm and at fluences of 1.1, 1.2, 1.3 and 1.4 Jcm^{-2}. The sections of the sample irradiated with 1.1, 1.2 and 1.4 Jcm^{-2} have very similar profiles, suggesting that the damage of each is the same, this being independent of the fluence of the laser pulse. The profile for the region of the sample irradiated with 1.3 Jcm^{-2} seems to extend slightly deeper and has a higher S_{peak} than the other three fluences. As it sits out of sequences with the other three, it seems more than likely that this behaviour is as result of errors in the annealing process at this particular fluence.

A possible explanation for the homogeneity of the type of damage caused may be due to the bond energy in 4H-SiC being about 5.5eV, this being equivalent in energy to the 193nm ArF pulses, suggesting the laser contributes directly to bond breaking by photon interaction. The resulting amorphisation (bond breaking at

high temperatures) creates vacancy agglomerates which readily trap positrons. Figure 7.1(b) shows PL spectra taken for the four radiation fluences as shown in figure 7.1(a). At the lowest fluence the effect of the radiation is to increase the broad band emission centred on ~490 nm, but from 1.2 Jcm^{-2} upward the effect is to reduce the intensity of all emissions.

The emissions centred on ~490 nm suggest similar kinds of radiative centres formed from the irradiation at all fluences; the decreasing intensities point to an increase in the number of laser induced defects. Both the PAS and PL spectra show the presence of defect regions resulting from laser irradiation; however, whereas the positron data suggests that the damage from each fluence is similar in both type and quantity of defect, the PL seems to point at a general increase in damage with increasing irradiation fluence. This may be indicative of the upper limit of positron sensitivity in differentiating between a high density of vacancy-type defect agglomerates.

7.3.2 Laser Annealing by 308nm Pulses

The remaining two wafers of 4H-SiC, namely 2a and 2b, were irradiated with 50 pulses of a XeCl laser, of λ=308nm, at fluences of 1.1, 1.2, 1.3, 1.4, 1.5, 1.6 and 1.8 Jcm^{-2}, with one quadrant of sample 2a left unirradiated, so that it would act as a reference sample. The S-parameter profiles and photoluminescence spectra for these samples can be seen in figures 7.2(a) and (b). The first thing that one notices about the S data is that there is a marked increase in S_{peak} for samples irradiated between fluences of 1.3 and 1.4 Jcm^{-2}, suggesting that this is the threshold region for vacancy formation. It is thought that when SiC is irradiated with pulses of this wavelength, that any bonds broken, and subsequent

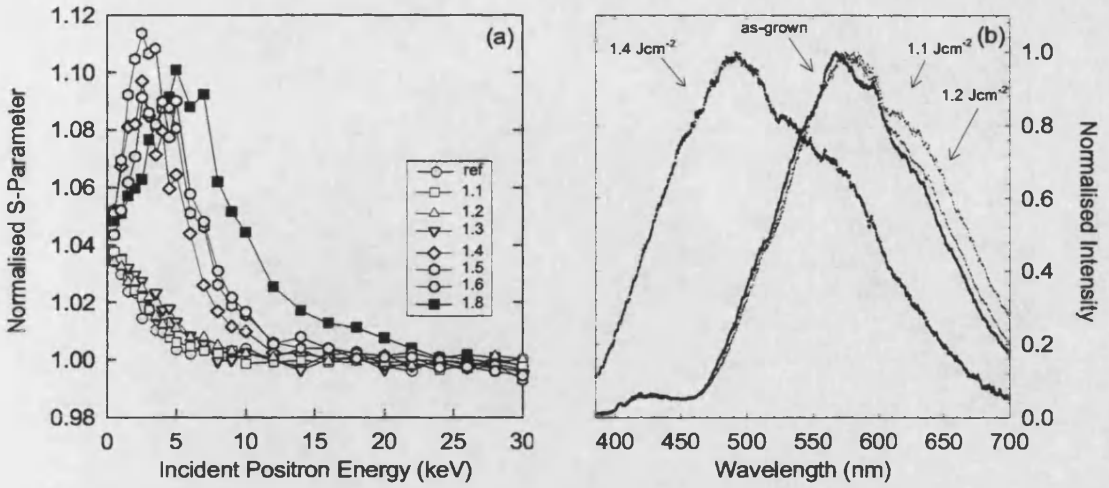

Figure 7.2: (a) Normalised S-Parameter profiles of two wafers of 4H-SiC irradiated with laser pulse of λ=308nm, varying fluences. (b) Photoluminescence spectra taken on the aforementioned samples irradiated at 1.1, 1.2 and 1.4 mJcm^{-2}, and one unirradiated sample.

vacancies created, are as a result of a purely thermal effect, as opposed to direct bond breaking caused by the 193nm ArF pulses, as seen in sample 1. Figure 7.2(b) shows a sudden transition consistent with the threshold observed in the PAS data, showing a shift of the broad band region from around 575nm for the undamaged sample irradiated at 1.2 Jcm^{-2} to the broad band being centred on 490nm after having been irradiated with 1.4 Jcm^{-2}. It is interesting to note that the broad band centre for sample 2 is the same as exhibited by sample 1, suggesting similar types of radiative centres in both samples, and, hence, similar defect structures[61]. In figure 7.2 one notices that the peak for the 1.8 Jcm^{-2} wafer is far broader than the other samples, with the damage extending far deeper into the sample. this suggest that not only is there a threshold fluence for vacancy formation using this particular wavelength of laser, but that the amount of damage caused is related to the fluence also.

Sample Irradiation Wavelength and Fluence (Jcm^{-2})	Box Depths (nm)	Defect Concentration (cm^{-3})
193nm		
1.1, 1.2, 1.3, 1.4	50, 100, 650	4×10^{19}, 2×10^{20}, 2×10^{19}
308nm		
Ref, 1.1, 1.2, 1.3	Undefected	Undefected
1.4, 1.6	50, 100, 800	4×10^{18}, 3.2×10^{20}, 2×10^{18}
1.8	100, 100, 200, 550	2×10^{19}, 2×10^{20}, 2×10^{19}, 2×10^{18}

Table 7.2: Results of fitting S profiles using POSTRAP assuming a specific trapping rate consistent with an agglomeration of eight divacancies. The data has been fit using several defect regions, each with a certain depth. The second column should be read as showing the widths of adjacent slabs, starting from the surface and moving towards the bulk.

7.3.3 Fitting Defect Profiles

When fitting defect profiles for vacancy type defects in silicon $S_{peak} \leq 1.036$, unless the sample has become amorphised. At first sight, it was felt that the S_{peak} value seen in figures 7.1 and 7.2 was indicative of amorphisation of the sample. However, Anwand *et al.* [62] postulate that a relationship exist between S/S_B and the number of divacancies in an agglomerate in which the positron is trapped. Accordingly, a value of 1.10 would correspond to an agglomeration of eight divacancies.

In order to fit the data for all the samples using POSTRAP a value for the specific defect trapping rate μ is needed, and assuming that the defects could be represented by agglomerates of eight divacancies a value 16 times that for Si monovacancies ($3 \times 10^{14} s^{-1}$) was used. The positron diffusion length for undefected SiC, also needed for POSTRAP, was found to 100nm. The results of the fitting can be found in table 7.2.

The majority of the defects appear to reside in a 50-nm-wide buried layer, about 70 nm below the surface. The optical penetration depth is ~200 nm and the thermal profile extends to ~2-3 μm; however, the latter profile is a sharp function of time.

7.4 Conclusions

The work described in this chapter demonstrates that open-volume defects are created by laser irradiation of SiC samples, both from direct bond breaking and from, more interestingly, thermal effects. The quantification of these effects has been mainly based on models developed over the years that describe defects with Si and SiC - and then never as a result of laser irradiation - and so act as only a tentative guide. However, the presence of large, agglomerated positron trapping sites beneath the surface is indisputable.

It is not certain why the damage caused by 308nm irradiation has a maximum below the surface. The irradiation is close to the ablation threshold, and the near-surface temperature during irradiation is expected to rise to close to 1700°C. The higher temperature at the surface could lead to preferential damage recovery; subsequent cooling at the surface is rapid, and it is thus possible that damage created in the sub-surface region will not have time to be repaired (in effect being frozen in). Optical microscopy of the treated surface shows no evidence of substantial surface damage associated, for example, with evaporation. Surface melting of SiC is not expected thermodynamically. One or two monolayers at most may leave the surface during irradiation, leaving crystalline material behind. The author therefore believes that the most likely explanation of the positron

results is based in the formation of subsurface vacancy agglomerates.

Chapter 8

Summary

There has been a great deal of work carried out on the slow positron beam, both at the University of East Anglia and at the University of Bath, over the past few years. The aim of this thesis is to highlight some of the interesting and innovative techniques that have been employed to yield, hopefully, data of scientific worth.

In chapter 4, the structural damage caused by the implantation of 5 keV B^+ into Fz-Si was investigated. By looking at such a low energy, low dose implant, we were studying the physical limit of device-fabrication technology. It is at this threshold that depth-resolved information is very important to the people making the next generation of electronic devices. In order to reduce the loss of resolution inherent with broadening of the positron implantation profile at higher energies, controlled etching of the sample to known depths was performed. The thickness to be etched was determined from the depth of the peak of the damage given by the output of the ion-implantation simulation code TRIM. However, the positron data showed there to be damage still present after etching, showing that the

TRIM code was unable to fully account for the full extent of the damage. PAS was also used in a complementary fashion alongside the established technique of SIMS. It was able to show that the defect profile extends further than that of the ions, something that was unexpected but very interesting, and important technologically. To the author's knowledge PAS is the only technique capable of shedding light on this phenomenon,

Chapter 5 was concerned with trying to find a pattern to the damage caused by the implantation of ions into matter. Data was taken for several different ions, implanted at various energies, various fluences and at varying currents all implanted into separate wafers of FZ-Si. By normalising $S(E_{peak})/S(E_{virgin})$ using vacancy-type defect values given by TRIM, it was shown that the implanted samples shared similar structures, although the implant conditions for each were vastly different from one another. In order to define a universal $S(C)$ curve from which it would be possible to predict defect concentration for any ion, of any energy and dose, a lot more data needs to be taken. At the time of writing, the positron research group at the University of Bath is in the process of constructing a compact spectrometer for ion dosimetry and uniformity mapping across Si wafers. The beam is intended to work at a high data collection rate, meaning short run times and thus speeding up the data acquisition process for formulating an $S(C)$ curve that could be applied to all the major dopants used in Si.

Chapter 6 described the first instance, to the author's knowledge, of in-situ annealing PAS studies of near-surface defects resulting from ion-implantation. We witnessed defect migration, using several different methods, namely S-parameter variations, changes in count rate and the variation of Ps fraction. Although the different techniques varied in their quantitative interpretation of the data, they

all pointed unanimously to a threshold temperature for the migration of defects created in self-implanted Si of $500^{o}C$, this being considerably higher than that expected. Now that the technique has been modified and has proven to be valuable in relaying information on the migratory behaviour of defects over a range of temperatures, the setup now exists to perform measurements on samples implanted with different ions, at varying doses in order to ascertain if there are any common annealing patterns.

Chapter 7 detailed an investigation into the damage created in 4H-SiC by laser irradiation at two wavelengths, an as-yet untried means of structure manipulation. PAS was able to demonstrate the existence of vacancy-type structures, with the 193nm wavelength irradiation contributing directly to bond-breaking, whereas the 308nm wavelength created defects via a thermal effect. The PAS data is corroborated in part by the PL data, with both techniques indicating the absence of elements on the crystal lattice; the PL data, however, suggests that the density of the defects caused by the 193nm irradiation is increasing with increasing fluence, whereas the PAS data is not sensitive to this change (beyond the saturation limit). An agglomerated divacancy model has been used to elucidate a quantitative fit from the PAS data.

Throughout the duration of this PhD, data has been taken on many more samples than are described in this thesis. The investigations described in this thesis were chosen to demonstrate the novel techniques and approaches that were used in conjunction with the established positron method in the past three years to draw out fresh and interesting information. Some of these advances - particularly those related to ion dosimetry and in-situ annealing - will form the basis of extensive further research in the Bath positron laboratory.

References

[1] P.A.M. Dirac. *Proc. Cambridge Philos. Soc.*, 26:361, 1930.

[2] S. Dannefaer. *Radiat. Effects and Defects in Solids*, 111-112:65, 1989.

[3] P. J. Schultz and K. G. Lynn. *Rev. Mod. Phys*, 60:701, 1988.

[4] *Positron Solid State Physics.* Proceedings of the International School of Physics 'Enrico Fermi' Course LXXXIII. edited by W. Brandt and A. Dupasquier, North Holland, Amsterdam, 1983.

[5] *Slow Positrons in Surface Science.* Proceedings of the International Workshop. edited by A. Vehanen, Pajulathi, Finland (Helsinki University of Technology), 1984.

[6] L. Madansky and F. Rasetti. *Phys. Rev.*, 79(397), 1950.

[7] C.D. Anderson. *Phys Rev*, 41:405, 1932.

[8] M. Deutsch. *Phys. Rev.*, 82:455, 1951.

[9] A.P. Mills Jr. *Phys. Rev. Lett.*, 41:1828, 1978.

[10] M.J. Puska. *J. Phys.: Condens. Matter*, 3:3455, 1991.

[11] R.C. Dynes J.P. Garno C.I. Westbrook, D.W. Gidley and J.M. Gibbson. *Appl. Phys. Lett*, 50:95, 1989.

[12] A.P Mills Jr. *Experimentation with Low Energy Positron Beams*, volume Proceedings of the International School of Physics 'Enrico Fermi' Positron Solid State Physics. edited by W. Brandt and A. Dupasquier, North Holland, Amsterdam, 1983.

[13] J. Szymański A.B. Walker, K.O Jensen and D. Neilson. *Phys. Rev. B*, 46(1687), 1992.

[14] K. O. Jensen P. G. Coleman, L. Albrecht and A. B. Walker. *J. Phys.: Condens. Matter*, 4:10311, 1992.

[15] J. P. Carbotte and H. L. Arora. *Can. J. of Phys.*, 45:387, 1967.

[16] S. Valkealahti and R. M. Nieminem. *Appl. Phys. A*, 32:95, 1983.

[17] N. B. Chilton P. G. Coleman and J. A. Baker. *Mater. Sci. Forum*, 105–110:213, 1992.

[18] K. G. Lynn A. Vehanen Nielsen, Bent and P. J. Schultz. *Phys. Rev. B*, 32:2296, 1985.

[19] P. Hautojärvi J. Mäkinen, C. Corbel and D. Mathiot. *Phys. Rev. B*, 42:11166, 1990.

[20] C.H. Hodges. *Phys. Rev. Lett*, 25:284, 1970.

[21] B. Y. Tong. *Phys. Rev. B*, 5:1436, 1972.

[22] J.A. Eady I.K. MacKenzie and R. R. Gingerich. *Phys. Lett. A*, 33:279, 1970.

[23] P. L. Jones P. H. Leo, K.D. Moore and F. H. Cocks. *Phys. Status Solidi B*, 108:K145, 1981.

[24] P. J. Simpson P. G. Coleman R. D. Goldberg, A. P. Knights. *J. Appl. Phys.*, 86:342, 1999.

[25] E. Soininen H. Huomo, A. Vehanen. *Appl. Phys. A*, 49:647, 1989.

[26] G. R. Heyland K. S. Lines M. Charlton, T. C. Griffith and G. L. Wright. *J. Phys. B*, 13:L757, 1980.

[27] A. Goodyear. *Sample Holder and Electron Beam Heater*, volume Version 2.1. University of East Anglia, Norwich, NR4 7TJ, 1995.

[28] T. Ohshima Y. Aoki M. Yoshikawa I. Nashiyama H. Okumura S. Yoshida T. Moriya T. Kawano A. Uedono, H. Itoh and S. Tanigawa. *J. Appl. Phys.*, 35(5986), 1993.

[29] Canberra Germanium Detector: GR2520, 73% efficiency.

[30] Ortec Amplifier Model 572.

[31] Ortec Model Model 459.

[32] Canberra ADC Model 8075.

[33] Canberra Digital Stabilizer Model8232.

[34] PC-LabCard. PCL-726 Six Channel D/A Output Card.

[35] 16k channel available Canberra-Packard System 100 MCA board.

[36] J. de Vries. R. A. Hakvoort M. R. A. van Veen, H. Schut. and Ijpma. *Positron beams for solids and surfaces,*, page 171. edited by P J Schultz, G R Massoumi and P J Simpson, AIP, New York, 1990.

[37] G. Aers. *Positron beams for solids and surfaces*, page 162. edited by P J Schultz, G R Massoumi and P J Simpson, AIP, New York, 1990.

[38] F. Priolo S. Libertino S. Coffa, V. Privitera and J. Mannino. *J. Appl. Phys.*, 81:1639, 1997.

[39] S. Cofa F Priolo S. U. Campisano K. Larsen Kyllesbech, V. Pribitera and A. Carnera. *Phys. Rev. Lett.*, 76:1493, 1996.

[40] K. G. Lynn P. Asoka-Kumar and D. O. Welch. *J. Appl. Phys.*, 76:4935, 1994.

[41] J.P. Biersack J. F. Ziegler and U. Littmark. *The Stopping and Range of Ions in Solids.* Pergamon, New York, 1985.

[42] M. Zinke-Allmang A. P. Knights, G. R. Carlow and P. J. Simpson. *Phys. Rev. B.*, 54:13955, 1996.

[43] M.Fujinami and N. B. Chilton. *J. Appl. Phys.*, 79:9017, 1993.

[44] E. Chason *et al. J. Appl. Phys.*, 81:6513, 1997.

[45] C. Jeynes P. G. Coleman A. Nejim, A. P. Knights and C. J. Patel. *J. Appl. Phys.*, 83:3565, 1998.

[46] J. Keinonen. *Phys. Rev. B*, 37:8269, 1988.

[47] A. Uedono *et al. Jpn. J. Appl. Phys.*, 44:1867, 1990.

[48] P. J. Simpson *et al. Phys. Rev. B*, 44:12180, 1991.

[49] R. Krause-Rehberg and H. S. Leipner. *J. Appl. Phys.*, 81:1639, 1997.

[50] X. T. Meng and W. J. Puff. *J. Phys.: Condens. Matter*, 6:4971, 1994.

[51] P. Hautojaärvi J. Mäkinen and C. Corbel. *J. Phys.: Condens. Matter*, 4:5137, 1992.

[52] K.O. Jensen and A. B. Walker. *J. Phys.: Condens. Matter*, 2:9757–9775, 1990.

[53] I. J. Rosenberg R. H. Howell and M. J. Fluss. *Phys. Rev. B.*, 34:3069, 1986.

[54] A. P. Knights and P. G. Coleman. *J. Phys.: Condens. Matter*, 7:6477–6482, 1995.

[55] Sigmaplot for Windows version 5.00 1986-1999 SPSS Inc.

[56] M. J. Puska. *Positron Annihilation*, page 101. edited by L. Vanpraet, M. Dorikens and D. Segers, ICPA VIII. World Science Publishing, Singapore, 1988.

[57] P. G. Coleman A. P. Knights F. Plazaola Y. Pacaud W. Skorupa J. Stärmer P. Willutski G. Brauer, W. Anwand. *Phys. Rev. B*, 54:3084, 1996.

[58] P. G. Coleman J. Stärmer F. Plazaola J. M. Campbell Y. Pacaud W. Skorupa G. Brauer, W. Anwand. *J. Phys.: Condens. Matter*, 10:1147, 1997.

[59] H. Itoh T. Ohshima Y. Aoki M. Yoshikawa I. Nashiyama H. Okumura S. Yoshida T. Moriya T. Kawano A. Uedono and S. Tanigawa. *Jpn. J. Appl. Phys.*, 35:5986, 1996.

[60] K. Abe H. Itoh Y. Aoki M. Yoshikawa S. Tanigawa T. Ohshima, A. Uedono and I. Nashiyama. *Jpn. J. Appl. Phys.*, 67:407, 1998.

[61] C. I. Harris A. O. Konstantinov, A. Henry and E. Janzén. *Appl. Phys. Lett*, 66:2250, 1995.

[62] P. G. Coleman R. Yankov W. Skorupa W. Anwand, G. Brauer. *Appl. Surf. Sci.*, 149:140–143, 1999.